

UNIVERSITY OF TWENTE

MASTER THESIS APPLIED MATHEMATICS

CHAIR MULTISCALE MODELING AND SIMULATION

# Direct Numerical Simulation of Bubble-Wall Interactions

*Author*

S.R. Ephrati

s1422197

*Supervisor*

Prof.Dr.Ir. B.J. Geurts

*Graduation committee*

Prof.Dr.Ir. B.J. Geurts

Prof.Dr.-Ing. J. Fröhlich

Dr. M. Schlottbom

July 22, 2019



## Preface

This master thesis concludes my graduation project and with it my time as a student. It closes off an enjoyable six years at the University of Twente during which I have left the lovely Friesland behind and have made the remote Enschede my home. Student life has allowed me to develop myself in a lot of ways to become the person I am today, to experience many exciting moments and activities, and to make many new friends with whom I have had a lot of fun over the years.

I would like to take this opportunity to thank several people. First of all I want to thank my supervisor prof. Geurts, who made it possible for me to go abroad during my internship and offered me this interesting subject to work on during my final year. During my final project I have often been amazed by the ability to untangle my thoughts and keep me busy for an entire week just by having a simple ten minute discussion.

I also want to thank prof. Fröhlich and Benjamin Krull for hosting me in Dresden and making me feel welcome in the Fluid Mechanics group. I have enjoyed the couple of months I spent in the group as well as the many discussions about serious and a little less serious subjects (mostly regarding cyclists and linguistic differences between German and Dutch). All in all, I look back at my time in Dresden with a very positive feeling.

I would also like to express my gratitude to Paolo Cifani, the developer of the TBFsolver. We have had quite some contact at the start of the project, when I had to learn how to use the program. Thank you for the quick responses to the (very) many e-mails I sent, and the time you have taken to explain me how to use the TBFsolver.

Needless to say I would like to thank my parents, without whom I would not have been able to study in the first place. You have invested a lot of time and effort in me, probably without even understanding what it actually is that I have been studying. Special thanks also go to my good friends David, Frank, Sander, Rico and Mike, with whom I have enjoyed many cups of coffee and many beers over the years.

Finally, I want to thank the members of the graduation committee for taking the time and effort to read and evaluate my work.



## Abstract

The motion of a bubble impacting on a solid wall is studied numerically using the open-source code TBFsolver for the simulations of multiphase flows. This code employs Direct Numerical Simulation (DNS) using a volume of fluid (VOF) approach, and has already been tested for situations involving a single bubble as well as a vast number of bubbles. An extensive study is performed for a single bubble hitting a wall head-on and under an angle of 45 degrees. Bubble movement and deformation suggest that the small-scale processes that occur during bubble-wall interactions are captured well by the solver. Geometric quantities along with the energy dissipation near the bubble are compared to an existing bubble collision model.

A method to approximate the flow between the bubble and the wall is presented using lubrication theory. This method is applied to numerical simulation results. The outcomes are found to be in qualitative agreement with the numerical simulation data. We conclude by discussing the possibilities of applying lubrication theory to the TBFsolver.



# Contents

<b>Preface</b>	<b>i</b>
<b>Abstract</b>	<b>iii</b>
<b>1 Introduction</b>	<b>1</b>
1.1 Multiphase flows and the importance of DNS . . . . .	1
1.2 Goal and structure of this study . . . . .	1
1.3 Criteria for the comparison of multiphase flow solvers . . . . .	2
1.4 Variables and notation . . . . .	2
<b>2 Description of the TBFsolver</b>	<b>3</b>
<b>3 Bubble-wall interactions</b>	<b>5</b>
3.1 Introduction . . . . .	5
3.2 Recreating the case of Heitkam et al. . . . .	6
3.3 Testing the assumptions of Heitkam et al. . . . .	10
3.4 Results 45 degree case . . . . .	13
3.5 Results 0 degree case . . . . .	18
3.6 Concluding remarks . . . . .	21
<b>4 Lubrication theory</b>	<b>23</b>
4.1 Nondimensionalization of the Navier-Stokes equations . . . . .	23
4.2 Simplification of nondimensionalised Navier-Stokes equations . . . . .	25
4.3 Finding the lubrication pressure . . . . .	28
4.4 Lubrication pressure in one-dimension . . . . .	29
4.5 Application to explicitly defined interfaces . . . . .	32
4.6 Application to the case of Heitkam et al. . . . .	35
4.7 Application of lubrication theory to the TBFsolver . . . . .	39
4.8 Concluding remarks . . . . .	40
<b>5 Conclusions</b>	<b>41</b>
<b>6 Discussion and recommendations</b>	<b>43</b>
<b>Bibliography</b>	<b>45</b>
<b>A Nomenclature</b>	<b>47</b>
A.1 Variables and vectors . . . . .	47
A.2 Dimensionless numbers . . . . .	47



---

# 1 Introduction

## 1.1 Multiphase flows and the importance of DNS

This master thesis deals with numerical simulations of multiphase flows, where multiple fluid phases are present. These flows occur in many industrial situations and play an important role in many applications, such as vaporization and combustion of dense sprays, or heat exchangers and cooling systems in industrial plants. A good understanding of these flows can be crucial for safety reasons in applications as cooling systems. Multiphase flows also occur in natural situations or situations closer to everyday life. Think of the formation of rain drops or bubbles in carbonated soft drinks.

A typical example which is often considered is that of bubbles of air dispersed in liquid water. In this situation the continuous phase, the phase that occupies a connected region of space, is water, and the dispersed phase, which occupies disconnected regions of space, is air. The simultaneous existence of multiple phases increases the complexity of the flow and introduces smaller time and length scales. For example, a thin liquid film remains between a bubble and an obstacle during an interaction, with a typical thickness many times smaller than the bubble radius.

Interactions between bubbles and obstacles frequently occur in multiphase flows when a large number of bubbles is present. These obstacles can be other bubbles, or the walls of the container or channel in which the bubbles move. This emphasizes the relevance of having an adequate knowledge of how these interactions take place and what their influence is on the flow.

The presence of multiphase flows in many practical applications stresses the importance of having a good understanding of the behaviour of these flows and the processes that take place within them. It is for this purpose that numerical simulations are used. Numerical simulations allow for control over a lot of variables, which might not always be the case in practical experiments. However, numerical simulations are built on mathematical methods which are subject to errors and it is for this reason that one should properly assess the credibility of the results.

One of the numerical methods used for simulating multiphase flows is direct numerical simulation (DNS). This method aims to computationally resolve the flow down to the smallest scales without the use of models to account for certain physical processes. Simply put, this means that a proper DNS of a multiphase flow yields the exact solution of the governing equations.

## 1.2 Goal and structure of this study

This study revolves around the TBFsolver, a program developed to simulate multiphase flows. The goal is to investigate bubble-wall interactions and compare the findings to existing collision models. The motivation for this is twofold. Firstly, extensively studying bubble-wall interactions with the TBFsolver grants new insights into these interactions and how the solver deals with these situations. Secondly, the strengths and weaknesses of existing collision models can be identified by comparing the results to DNS data. This in turn might result in improvements for the methods and for identifying the range of application in which the models can be used.

The structure of the thesis is as follows: section 2 briefly describes the TBFsolver to give an overview of the mathematical methods used in the program. In section 3 a comparison is made between a bubble-wall interaction as simulated with the TBFsolver and the predicted results

from an existing collision model. A theoretical approach to bubble-wall interactions is considered in section 4 by using lubrication theory and these results are subsequently compared to the data obtained from the TBFsolver. The thesis closes with the conclusions in section 5 and a discussion in section 6.

### 1.3 Criteria for the comparison of multiphase flow solvers

Several criteria are kept in mind when comparing the numerical methods, of which the most important ones are listed below.

- Stability
- Accuracy, which includes accurate flow computations and bubble deformations, and convergence rate of numerical solutions. both qualitatively and quantitatively
- Computational cost

Other points of interest are the effort required to add additional functionality to the solver and change the built-in functions and the ease with which relevant quantities can be calculated.

### 1.4 Variables and notation

Physical parameters are used throughout this thesis. These parameters can be viewed as if they are divided by the corresponding physical SI unit, therefore no units have been used in this report. This has been done because our interest lies not in the particular choice of physical parameters, but rather in the dimensionless numbers following from those parameters.

Vectors are denoted using bold characters. For example, we write  $\mathbf{u} = (u, v, w)$  to denote the velocity vector with components  $u, v$  and  $w$ . The reader is referred to appendix A for a list of variables and dimensionless numbers.

The continuous phase is often referred to as the 'liquid' throughout this thesis, the dispersed phase is commonly called the 'bubble' consisting of 'gas'.

---

## 2 Description of the TBFsolver

The TBFsolver is the numerical code with which the simulation data throughout this report is obtained. A brief description of the governing equations and numerical algorithm are provided for completeness. The description closely follows along the lines of Cifani [6], for a full description the reader is referred to Cifani [6] and Cifani et al. [5].

### Governing equations

The numerical technique used in the TBFsolver is the volume of fluid (VOF) method. The mathematical model for multiphase flows follows the one-fluid formulation, i.e., a single set of equations is solved on the entire domain and material properties and interfacial terms are accounted for using a marker function  $f$ . Each bubble is given a marker function  $f_i$  which equals 1 in cells where the bubble fully occupies the cell, 0 where the fluid occupies the cell, and a value between 0 and 1 indicates that the cell contains a bubble interface. The value of the marker function is also referred to as the volume fraction. Given  $N$  bubbles, the marker functions are advected via

$$\frac{\partial f_i}{\partial t} + \mathbf{u} \cdot \nabla f_i = 0 \quad \text{for } i = 1, \dots, N. \quad (1)$$

The nondimensionalized incompressible Navier-Stokes equations and incompressible continuity equation are used to describe the flow:

$$\rho \left( \frac{\partial \mathbf{u}}{\partial t} + \nabla \cdot (\mathbf{u}\mathbf{u}) \right) = -\nabla p + \frac{1}{\text{Fr}^2} \rho \hat{\mathbf{g}} + \frac{1}{\text{Re}} \nabla \cdot (2\mu \mathbf{D}) + \frac{1}{\text{We}} k \mathbf{n} \delta(n) \quad (2)$$

$$\nabla \cdot \mathbf{u} = 0 \quad (3)$$

Here  $\mathbf{u}$  is the velocity,  $t$  is the time,  $p$  is the pressure,  $\rho$  the density,  $\mu$  the viscosity,  $k$  is the curvature,  $\hat{\mathbf{g}}$  is the normalized gravity vector,  $\mathbf{D}$  the deformation tensor, and  $\mathbf{n}$  is the normal vector to the interface. The dimensionless numbers are the Froude number  $\text{Fr} = U/\sqrt{gL}$ , the Reynolds number  $\text{Re} = UL\rho_1/\mu_1$ , and the Weber number  $\text{We} = LU^2\rho_1/\sigma$ . Here  $L$  and  $U$  denote a characteristic length and a characteristic velocity, respectively. The subscript 1 denotes the continuous phase.

The Froude number is defined as the ratio between inertial forces and gravitational forces. The Reynolds number gives the ratio between inertial forces and viscous forces. A small Reynolds number indicates that viscous forces dominate and generally occurs in laminar flow, whereas a large Reynolds number characterizes turbulent flow. The Weber number is a measure of the importance of the inertia of the flow compared to the surface tension. Strong bubble deformation is typical for high Weber numbers.

The density and viscosity at a certain point follow from the marker functions and the properties of the continuous and dispersed phases. For instance, a cell with volume fraction value  $c$  would have a density and a viscosity of

$$\rho = \rho_1 (1 - c) + \rho_2 c, \quad (4)$$

$$\mu = \mu_1 (1 - c) + \mu_2 c. \quad (5)$$

## Discretization of surface tension and interface curvature

The continuous surface force (CSF) method [4] is used to model the surface tension term. This method replaces the delta function  $\delta(n)\mathbf{n}$  by a smooth term, which is computationally easier but also suffers from spurious currents. These spurious currents are unphysical velocities generated by the discretisation of the surface tension.

Reducing spurious currents can effectively be done by accurately computing the curvature of the interface [9]. The TBFsolver uses a height function method for this purpose. This method constructs a local height function from the volume fraction in the computational cells and differentiates this function to obtain the curvature. The reader is referred to Cummins et al. [7] for a detailed description of this method.

## Spatial discretization

A three-dimensional Cartesian grid is used to discretize the domain. A uniform grid in all directions is chosen throughout this report. The TBFsolver currently offers both collocated and staggered arrangement of the variables. However, a staggered arrangement was the only available option at the time at which most of the tests in this report were performed. The velocity components are then defined on the cell edges, the pressure and the volume fraction field are defined at the cell centers. This arrangement ensures a strong coupling between pressure and velocity [5].

The spatial discretization of the convective term in equation (2) is based on the finite volume approach. Additionally, the QUICK interpolation scheme [15] is implemented in the TBFsolver and has been used for the simulations in this report. This scheme avoids the presence of unphysical oscillations that occur for increasing Reynolds numbers [16]. A second order finite difference scheme is employed for the diffusive term.

## Temporal discretization

A third-order Runge-Kutta scheme is used to discretize the convection and diffusion terms of the Navier-Stokes equations, a Crank-Nicolson scheme is employed for the surface tension term. The time integration follows a fractional step approach, in which each time step is composed of three stages  $t^s$ . Here we have that  $s = 0$  corresponds to time step  $t^n$  and  $s = 3$  corresponds to the new time step  $t^{n+1}$ . The following actions are performed per stage  $t^s$ .

- The marker functions are advected and the bubble interface is reconstructed, yielding  $f$  at  $t^{s+1}$ .
- A provisional velocity  $\mathbf{u}^*$  is obtained, based on the velocities of the previous stages and the material properties of the previous and the current time step.
- The pressure in the new time step is calculated by solving a Poisson equation, using the provisional velocity.
- A correction based on the newly acquired pressure is applied on the velocity to obtain a divergence-free velocity field.

---

## 3 Bubble-wall interactions

### 3.1 Introduction

It is very likely that bubbles interact with each other or with walls when considering a turbulent flow with a large number of bubbles. The bubble seems to be in contact with the obstacle during such interactions, though this is not the case. A thin liquid film, a 'lamella', remains inbetween the objects, which causes a bounce when the thickness remains above a certain threshold. Rupture of the film results in coalescence in the case of a bubble-bubble interaction [19]. In this section we will only consider bouncing as the outcome of the interactions, since bubble coalescence is not included in the TBFsolver.

The presence of the liquid film between the bubble and the obstacle introduces small length scales into the flow. For example, bubble coalescence takes place when the thickness of the film reaches a molecular interaction range [20], which typically is of the order of  $10^2 \text{ \AA}$  ( $10^{-8}$  meter) [17]. Fully resolving these newly introduced length scales requires a very fine grid, which is practically infeasible even when simulating a single bubble. Hence it is desirable to introduce a model which captures the small-scale processes and eliminates the need for a very fine grid. This requires knowledge of the processes taking place during interactions in order to argue which of those processes can be neglected or approximated without severely deteriorating the quality of the solution.

The topic of this section is a rising bubble which at some point hits a wall. This problem is strongly related to the problem considered by Heitkam et al. [12]. This paper presents results of bubble-wall interactions using physical experiments as well as numerical experiments, and subsequently propose a collision model for small bubbles.

The first numerical experiment performed in this section considers three cases of a bubble interacting with a wall due to gravity and is similar to the physical experiment performed in the mentioned paper. This experiment demonstrates that a meaningful bubble-wall interaction is taking place at all and shows that the choice of parameters allows for a good comparison with the results of Heitkam et al.

The model of Heitkam et al. results in physical behaviour whilst requiring low computational effort. It is interesting to see how the physical model compares to results of simulations with the TBFsolver providing detailed resolutions of the bubble-wall interactions, and at which points the proposed model differs from the results of the TBFsolver. Moreover, the assumptions on which the model is based can be tested and possibly improved. This comparison is performed in the second numerical experiment, which consists of a detailed study of one of the cases of the first experiment.

The organization of this chapter is as follows: in section 3.2 we use the TBFsolver to numerically recreate the physical experiment performed by Heitkam et al. The setup for the comparison between the model of Heitkam et al. and the results of the TBFsolver is given in section 3.3. The numerical experiments used for testing the assumptions made by Heitkam et al. are performed in section 3.4 for the 45 degree case, and in 3.5 for the 0 degree case. Concluding remarks are given in section 3.6.

## 3.2 Recreating the case of Heitkam et al.

### Problem description and goal

The goal of this numerical experiment is to replicate the physical experiment performed in the reference paper. This has two main motivations. Firstly, it is important to know whether situations such as those considered by Heitkam et al. can be recreated properly by the TBFsolver. Secondly, successfully recreating the physical experiment allows us to continue studying the case in more detail and to extensively test the proposed model. Recreating the physical experiment is not trivial, since not all required dimensionless variables are stated in the reference paper and the parameter choice influences the stability of the simulation.

Three different cases are simulated using the TBFsolver, with a set of parameters based on the information provided in the paper of Heitkam et al. The results are compared and subsequently a single set of parameters is chosen for further comparison in the next section.

### Numerical setup

The initial configuration is shown in figure 1. This figure shows a two-dimensional slice of the domain parallel to the  $xy$ -plane.

The domain is a cuboid tank with a solid top and bottom, and periodic boundaries on the side. An inclined wall at the top of the domain is achieved by changing the direction of gravity, i.e. by changing the value of  $\alpha$ . The value of  $\alpha$  equals the angle the direction of gravity makes with the  $y$ -axis, with  $\alpha = 90^\circ$  corresponding to gravity being parallel to the  $x$ -axis.

The bubble is initially spherical with radius  $R = 0.5$  and is placed such that the distance between the center of mass of the bubble and the top wall equals  $11.3R$  in the direction of gravity, equal to the initial position of the bubble in the numerical experiment performed in the reference paper. This distance is denoted by  $L_c$  in figure 1. The entire domain is a cube with a length of  $12.8R$  in each direction. A grid with 128 cells in each dimension is employed, corresponding to 10 grid cells per bubble radius. This is denoted by  $R/h$  in table 1 and the chosen grid is sufficiently fine to properly resolve the shape of a deforming bubble [6].

The parameters used for the cases are given in table 1. The density and viscosity ratios are equal to those of air and water, where water represents the continuous phase and air the dispersed phase. The Eötvös number and the Reynolds number are given in the reference paper, but the latter is an output parameter rather than an input parameter. For this reason the Galilei number is used, which can be determined a priori. This number represents how quickly the bubble will accelerate due to the density differences of the phases. The value of the Galilei number is varied throughout the test cases by varying the viscosities. The Eötvös number gives the ratio between gravitational forces and surface tension forces and serves as a measure of how easily a bubble deforms. A higher value of the Eötvös number indicates that the bubble is not easily deformed.

Table 1: Numerical simulation setup and material properties.

Test case	$R$	$\rho_1$	$\rho_2$	$\mu_1$	$\mu_2$	$g$	$\sigma$	$R/h$	$\Delta t$
3.1	0.5	9.97	$1.18 \times 10^{-2}$	$6.87 \times 10^{-2}$	$1.43 \times 10^{-3}$	1	20.7	10	Adaptive
3.2	0.5	9.97	$1.18 \times 10^{-2}$	$7.66 \times 10^{-2}$	$1.59 \times 10^{-3}$	1	20.7	10	Adaptive
3.3	0.5	9.97	$1.18 \times 10^{-2}$	$7.11 \times 10^{-2}$	$1.48 \times 10^{-3}$	1	20.7	10	Adaptive

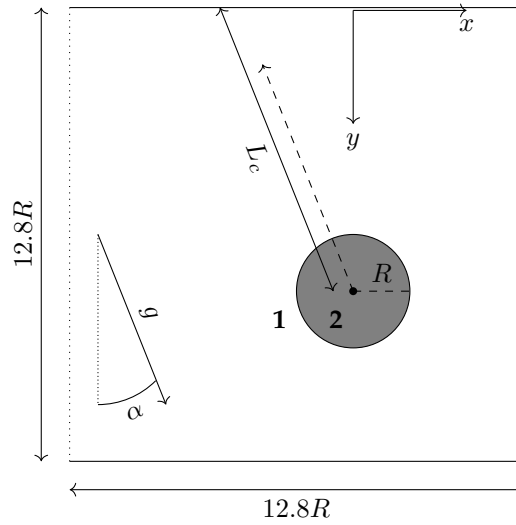


Figure 1: Initial configuration. The bold numbers indicate the phases.

The following dimensionless numbers are used to describe the test cases.

- Density ratio  $\rho_1/\rho_2$ ;
- Viscosity ratio  $\mu_1/\mu_2$ ;
- Eötvös number  $\text{Eo} = (\rho_1 - \rho_2)gL^2/\sigma$ ;
- Galilei number  $\text{Ga} = \rho_1\sqrt{|\rho_2/\rho_1 - 1|gL^3}/\mu_1$ .

The characteristic length  $L$  is chosen as the bubble diameter. The values of these dimensionless numbers for the considered cases are given in table 2.

Table 2: Dimensionless numbers corresponding to the variables in table 1.

Test case	$\rho_1/\rho_2$	$\mu_1/\mu_2$	Ga	Eo
3.1	845	48	145	0.48
3.2	845	48	130	0.48
3.3	845	48	140	0.48

### Quantities of interest

Several quantities of interest are used for verifying whether the obtained data is genuinely DNS data, in the sense of fully resolving all dynamically relevant scales, and for testing the assumptions made by Heitkam et al. In the definitions below  $\Omega_2(t)$  is the domain occupied by the dispersed phase a time  $t$ , with  $|\Omega_2|$  being the corresponding volume.

- Bubble movement
  - Center of mass:  $\bar{\mathbf{x}}(t) = |\Omega_2|^{-1} \int_{\Omega_2(t)} \mathbf{x} \, d\mathbf{x}$ .
  - Velocity, in three directions:

- i)  $\bar{\mathbf{u}}_t(t) = |\Omega_2|^{-1} \int_{\Omega_2(t)} \mathbf{u}_x d\mathbf{x}$ , the velocity tangent to the wall,
- ii)  $\bar{\mathbf{u}}_n(t) = |\Omega_2|^{-1} \int_{\Omega_2(t)} \mathbf{u}_y d\mathbf{x}$ , the velocity normal to the wall,
- iii)  $\bar{\mathbf{u}} = \sin(\alpha)\bar{\mathbf{u}}_x + \cos(\alpha)\bar{\mathbf{u}}_y$ , the velocity parallel to the direction of gravity.

- Bubble deformation

- Bubble diameter:  $\mathbf{d}(t) = (d_1(t), d_2(t), d_3(t))$ , where  $d_i(t) = \max_{\mathbf{x}, \mathbf{y} \in \Omega_2(t)} |x_i - y_i|$ ,  $i = 1, 2, 3$ .
- Contact area with the wall, expressed as the radius  $R_a$  of the circle with the same area. The definition is discussed in section 3.3.

- Energy dissipation inside the fluid:  $\varepsilon = 2\frac{\mu_1}{\rho_1} S_{ij}^2$ ;  $S = \frac{1}{2} (\nabla \mathbf{u} + \nabla \mathbf{u}^T)$ .

The center of mass is calculated as the averaged integral of the position over the volume occupied by the bubble. The bubble velocity is calculated similarly using the velocity rather than the position. Integration is performed numerically using the trapezoidal rule. The diameter essentially is the maximum distance occupied by the dispersed phase in each spatial dimension. We are especially interested in the diameter increase during the collision process, for comparison with the model of Heitkam et al.

Determining whether the flow is fully resolved is interpreted here based on the normal distance between the bubble and the wall. We assume that the flow between the bubble and the wall can be properly resolved as long as this distance equals four grid cells.

The bubble movement is of importance, if the corresponding quantities have not converged we can assume the overall solution has not converged. Moreover, the lamella thickness is considered an important quantity, but properly measuring this quantity might not be possible because of it being smaller than the grid size.

The energy dissipation is calculated in multiple regions in the fluid, directly related to the bubble. The regions we consider are the entire fluid, the control volume and the fluid lamella, as shown in figure 2. The control volume is defined as the area between the bubble and the wall. Note that figure 2 exaggerates the thickness of the lamella for illustrational purposes; the actual lamella is many times thinner. Moreover, the control volume includes the lamella when the bubble is in the vicinity of the wall.

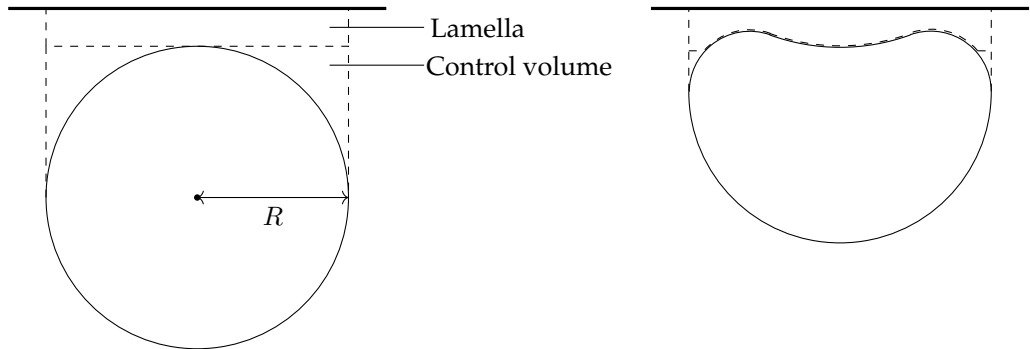


Figure 2: Sketch of the geometry. The right figure displays when the bubble is near the wall.

## Results

Figure 3 shows the bubble trajectories for the considered test cases. The trajectories are calculated by following the center of mass during the simulation. The dashed lines represent the bounds given by the experimental data presented in the reference paper. The blue line is the result of the collision model of Heitkam et al., this data was taken directly from the paper. The experimental data consists of measurements at different points in time, which have been performed for multiple bubbles separately. No trajectories have been reconstructed using this data, rather the entire set of measurements has been displayed. The experimental bounds have been deduced from this set by drawing upper and lower bounds which contain most of the measurements and suggest that that a single major bouncing event takes place.

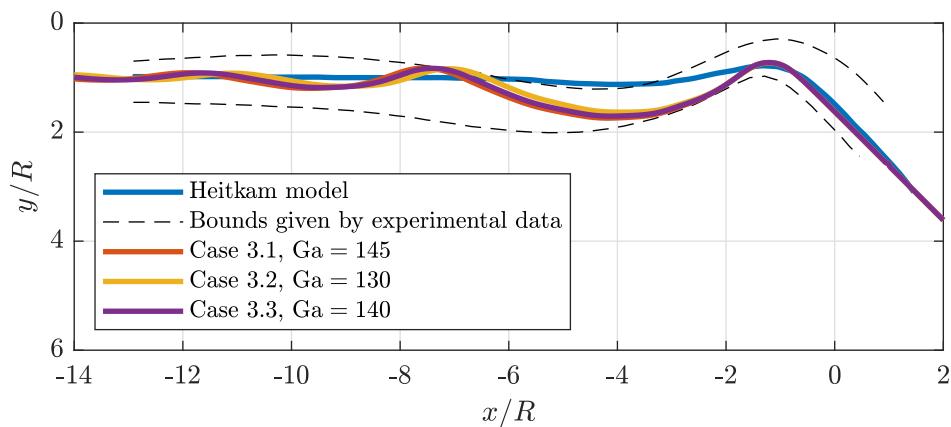


Figure 3: Trajectories for the different cases compared to the data from Heitkam et al.

### Interpretation of the bubble trajectories

Figure 3 shows that the results of the TBFsolver fit within the experimental bounds, as desired. In addition, it is clear that the results of the TBFsolver and the numerical results of Heitkam et al. differ strongly. The main cause is probably the rebound of the bubble after the initial contact with the wall. The simulation results from the TBFsolver suggest that a bouncing event takes place, whereas the numerical results of Heitkam et al. show the bubble interacting with the wall and sliding along the wall afterwards. Moreover, the initial rebound in the simulations of the TBFsolver results in several consecutive interactions with the wall, where each subsequent interaction yields a smaller bouncing event.

The results of the TBFsolver exhibit no significant differences amongst themselves. Figure 3 implies that a larger Galilei number results in a larger bubble rebound, which is to be expected since a large Galilei number implies a faster bubble acceleration due to the density differences of the phases. While the trajectories for  $Ga = 130$  and  $Ga = 140$  both still seem to fit inside the experimental bounds, the case of  $Ga = 145$  will be used in the next section to extensively study bubble-wall interactions.

### 3.3 Testing the assumptions of Heitkam et al.

#### Problem description and goal

We have shown before that the experimental results of the case of Heitkam et al. can be recreated using the TBFsolver. The goal now becomes to test some of the assumptions made by Heitkam et al. by using grid refinement for several cases.

The original approach was to use simple, inexpensive test cases which progressively get physically more relevant and harder to calculate. The idea behind this is that the fluid lamella that appears during a bubble-wall interaction is easier to fully resolve in non-physical test cases, so DNS data can be obtained. Results have shown that fully resolving this lamella with the TBFsolver is only possible when a situation without gravity is considered. However, these situations differ too much from the physically relevant cases and are therefore not considered useful.

Instead, the applied approach makes use of one of the situations used in the previous subsection. It is known that parts of the flow will not be properly resolved during a part of the bubble-wall interaction for this case. Nonetheless, the results can be compared for the parts of the simulation where the flow is fully resolved, i.e., where the smallest length scales of the flow are well resolved on the grid. Even though this means that no DNS data is obtained for the entire domain and the entire duration, we will still consider values of geometrical quantities of interest in order to test the assumptions made in the Heitkam paper.

Summarizing, by performing said simulations we hope to achieve the following goals.

- Obtain DNS data during the approach of the bubble to the wall and reliable data during the bubble-wall interaction.
- Use the data to find in which areas the simulation performed with the TBFsolver is not DNS and investigate how this influences the results of the simulations of the bubble-wall interaction.
- Use the obtained data to test and possibly improve the assumptions made in the reference paper.

#### Implementation of boundary conditions at the wall in the TBFsolver

The TBFsolver employs a contact-angle model to allow for physically relevant bubble-wall interactions [6]. This model is based on the work of Afkhami and Bussmann [2], and is briefly explained here for completeness.

The contact angle describes how the bubble interface should be reconstructed near the wall, more specifically, it describes towards which direction the interface normal should point for certain cells near the wall. The direction of the interface normal is uniquely determined by the contact angle in two-dimensional cases and is explained here. The idea for three dimensions is slightly more extensive but follows along the same lines.

The contact angle in two dimensions determines the interface normal as follows.

- A contact angle of  $0^\circ$  corresponds to interface pointing in the same direction as the wall normal, i.e., the bubble is directly in contact with the wall and the interfaces are parallel to each other.

- A contact angle of  $90^\circ$  means that the interface normal and the wall normal are perpendicular to each other, and therefore the bubble makes contact with the wall at an angle of  $90^\circ$ .
- A contact angle of  $180^\circ$  indicates that the interface normal and the wall normal point directly towards each other, which results in the presence of a film of fluid between the bubble and the wall.

As stated by Cifani [6], the choice of the contact angle only slightly affects the mean properties of the flow in turbulent channel bubbly flows, since it only affects the shape of the bubble in close proximity to the wall. However, a contact angle of  $180^\circ$  is implemented in the TBFsolver as a standard boundary condition choice for the volume fraction field to allow for physically relevant bubble-wall interactions. This is also the boundary condition which has been used throughout the simulations in this section.

### Definition of the fluid lamella

A thin film of fluid remains between the bubble and the wall during bubble-wall interactions. This film is experimentally shown to be approximately 30 to 100 times smaller than the bubble radius for some instances [19]. It should be noted that these values are measured for smaller viscosity ratios than the case considered in this report, but still provide us with an estimate of the thickness. We therefore assume that the lamella is contained within the first layer of cells adjacent to the wall on the coarsest considered grid ( $R/h = 10$ ) and the first refinement ( $R/h = 20$ ).

### Calculating the quantities of interest

An important quantity is the fluid lamella thickness. It is assumed that the interface near the wall is locally tangent to the wall, which means that the distance between the bubble and these cells is  $(1 - c)\Delta x$  if the cell has a nonzero volume fraction  $c$ . This is also in agreement with the boundary condition employed by the TBFsolver, and is assumed to give a good approximation of the local lamella thickness. Furthermore, the volume fraction in each cell is readily available from the TBFsolver.

It is unclear how to calculate the other quantities of interest which are related to the fluid lamella exactly. However, approximations for these quantities can be made and the results on different grids can be compared.

There are two problems we need to overcome when calculating the quantities of interest related to the fluid lamella. Firstly, it is unclear at which distance from the wall the bubble should be considered in contact with the wall, since it is known that fluid is always present between the bubble and the wall. In addition, it is unknown which distance between the bubble and the wall should exactly be considered as the fluid lamella when calculating the dissipation. Secondly, the flow in the fluid can not be calculated exactly in computational cells that contain the bubble interface. We elaborate on these points below.

A quantity related to the fluid lamella is the contact area with the wall. Since the bubble is never physically in contact with the wall, a definition of the contact area should be constructed. The only variable which can be used for this quantity is the volume fraction field. Therefore

we consider the bubble to be in contact with the wall, if the value of the volume fraction field is above a certain threshold value in a computational cell adjacent to the wall. We will denote this value by  $c_{th}$ . Note that a volume fraction of  $c_{th}$  in a cell adjacent to the wall implies that the local distance between the bubble and the wall is  $(1 - c_{th})\Delta x$ . Clearly, the contact area is dependent on the value of  $c_{th}$  and hence it is best to compare the results for multiple value of  $c_{th}$ .

When comparing the results on different grids, the value of  $c_{th}$  should be chosen per grid such that it agrees with the grid refinement. For example, if on a certain grid the value of  $c_{th}$  is known, the value used on a grid with a coarsening of a factor two in the wall-normal direction is  $0.5 + 0.5c_{th}$ . This idea is sketched in figure 4.

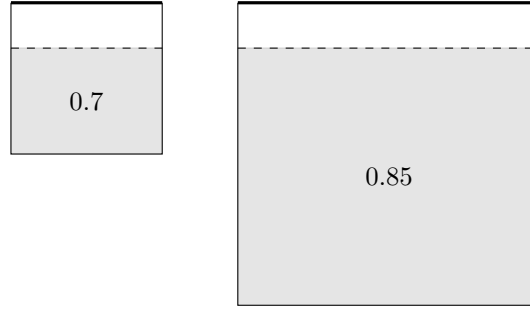


Figure 4: The same distance between the bubble and the wall on different grids can be compared by using the right values of the volume fraction field. This example shows that a value  $c_{th} = 0.7$  on the fine grid (left cell) corresponds to a value of 0.85 on the coarse grid (right cell).

A computational cell that contains the bubble interface is, by definition, partially filled with liquid and partially filled with gas. Hence the density and the viscosity in this cell are averaged based on the volume fraction field, as stated in equations (4) and (5). This causes the TBFsolver to regard the contents of this cell as a mixture of both phases when calculating the flow inside the cell. Thus it is impossible to find out how the flow behaves in each phase separately. Calculating the dissipation in the fluid is therefore not trivial in cells that contain the interface.

This becomes a problem when calculating the dissipation in the lamella. As stated before, the calculation of any quantity related to the lamella should be seen as an approximation and for that reason the dissipation in the lamella is calculated considering multiple values of  $c_{th}$  as the lamella. This grants an outline of the qualitative development of the dissipation inside the lamella over time, and provides an estimate for the actual dissipation taking place.

### Assumptions in the Heitkam paper used for comparison

Not only is it interesting to compare the results of the TBFsolver with those of the model of Heitkam et al, the results can also be used to test some of the assumptions on which the model is built. The following assumptions in the reference paper can be tested against the data obtained with the TBFsolver:

- The fluid lamella thickness  $h_0$ . The proposed model uses  $h_0 = \sqrt{\frac{3}{8}} \sqrt{\mu_1 U R^2 / \sigma}$ , which remains constant throughout the collision process. We take the wall-normal velocity of the bubble as the characteristic velocity  $U$ .

- The relation between the bubble deformation  $\Delta$  and the contact area radius  $R_a$ . The amount the sphere is deformed by the wall is represented by  $\Delta$ , given by

$$\Delta = R - y_c + h_0. \quad (6)$$

Note that  $y_c$  denotes the  $y$ -coordinate of the center of mass of the bubble and equals the minimal distance between wall and the center of mass and the bubble. The used relation between  $\Delta$  and  $R_a$  is

$$\frac{R_a}{R} = -30.0 + \sqrt{900.0 + 0.424 \frac{\Delta}{R}}. \quad (7)$$

- Energy dissipation in the fluid lamella. The model proposes that  $h_0$  remains constant throughout the collision process, which results in no dissipation inside the lamella but only near its rim.

### Grid refinement study

We consider two cases of bubble-wall interactions. The first one is as performed by Heitkam et al., where the bubble approaches the wall under an angle of 45 degrees. The second case considers the same material properties but the bubble approaches the wall head-on. The dimensionless numbers for these cases are given in table 3, these are the same parameters as used for test case 4.1, displayed in table 1. A  $128^3$  grid and a  $256^3$  grid are employed for both cases, a finer grid was not possible due to time limitations.

Table 3: Dimensionless numbers for case of Heitkam et al.

$\rho_1/\rho_2$	$\mu_1/\mu_2$	Ga	Eo
845	48	145	0.48

### 3.4 Results 45 degree case

Figures 5 to 6 show the movement of the bubble over time. The black dotted lines show at which point in time the bubble is within four grid cells of the wall for the first time. What stands out from these figures is the increase in the velocity both normal and tangential to the wall on the  $256^3$  grid compared to the  $128^3$  grid. Despite this difference, the  $y$ -center of mass in figure 6 over time shows good agreement between the two grids.

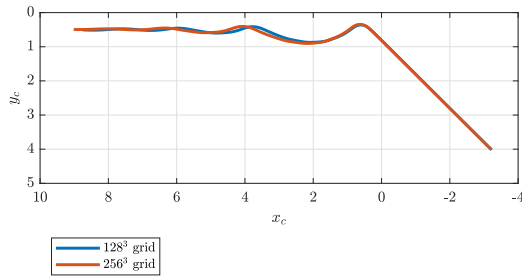


Figure 5: Bubble trajectory.

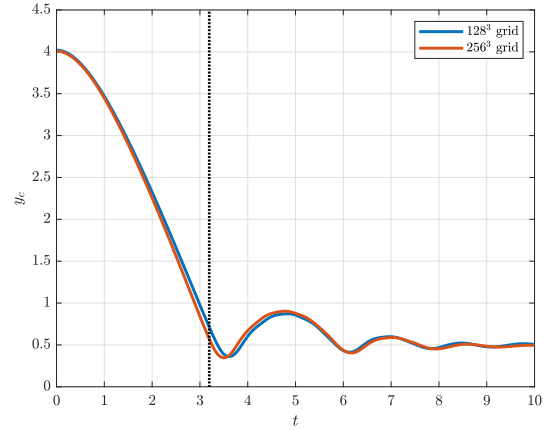
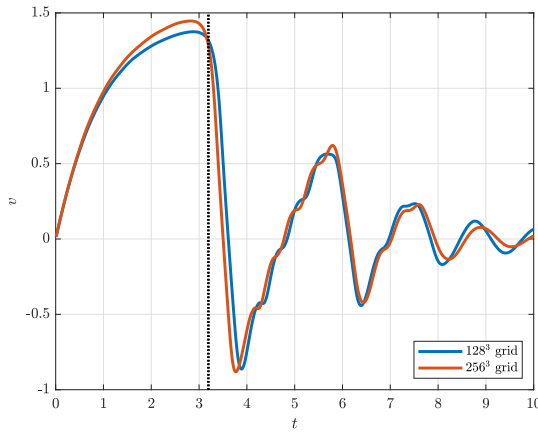
Figure 6:  $y$ -center of mass over time.

Figure 7: Velocity normal to the wall.

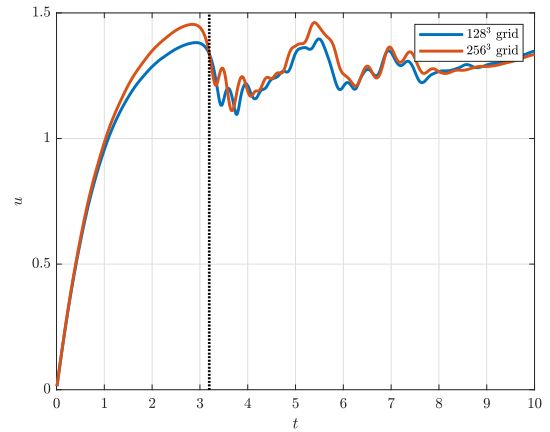


Figure 8: Velocity tangential to the wall.

### Comparison with the model assumptions

Figure 9 shows the minimal distance between the bubble and the wall. The dotted black lines are four times the grid sizes for both considered grids, the dashed yellow line represents the lamella thickness as expected from the Heitkam paper based on the bubble Reynolds number obtained from the TBFsolver. It is notable that the results of the TBFsolver on both grids show very little difference until the minimum distance is less than 0.5% of the bubble radius. The minimum thickness at this point exhibits relatively large fluctuations, which might be due to numerical inaccuracies. These observations lead us to conclude that the lamella thickness is not constant throughout the collision process. The variable lamella thickness in turn implies that energy dissipation does take place in the lamella.

The average energy dissipation per computational cell in the fluid is shown in figure 10. These values are calculated by integrating the dissipation over the desired volume and subsequently dividing by the occupied volume. The figure clearly shows at which points the bubble hits the wall, during which the energy dissipation is greatly increased. The increased bubble velocity

on the fine grid results in larger velocity gradients than on the coarse grid, which in turn yield a larger energy dissipation.

Figure 11 provides the energy dissipation in the control volume over time. The results on the used grids show the same developments. Approximately two-thirds of the overall dissipation in the fluid is taking place in the control volume during the initial contact. The remainder likely takes place in the wake of the bubble, which becomes more apparent after the initial contact when the wake starts to interact with the wall.

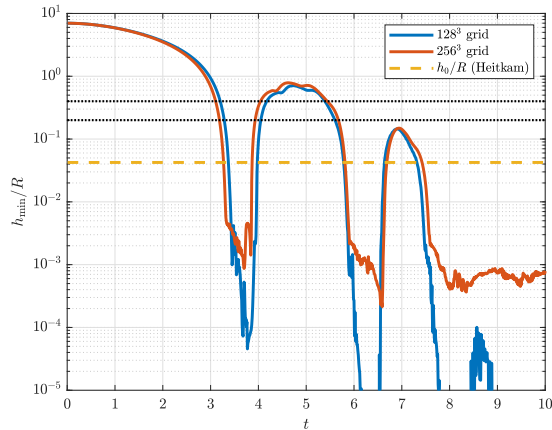


Figure 9: Minimum distance between the bubble and the wall.

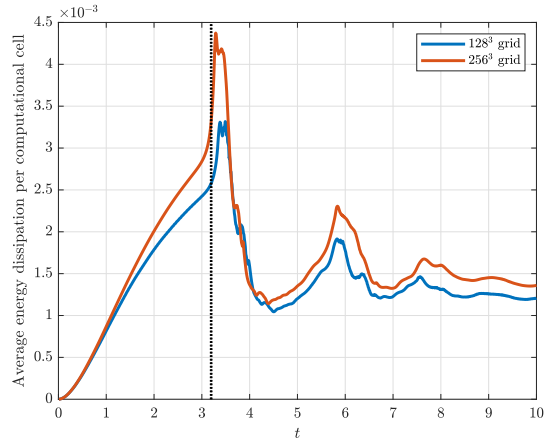


Figure 10: Energy dissipation in the entire fluid region.

The energy dissipation in the lamella for the  $256^3$  grid is given in figure 12. Even though it is not clear at which value of  $c_{th}$  the lamella is defined, it becomes clear from the figure that a significant fraction of the energy dissipation takes place between the bubble and the wall. This is likely caused by the sharp velocity gradient near the wall due to the no-slip boundary condition at the wall. The decrease of the dissipation in the lamella during the second contact with the wall is caused by the decrease of the wall-normal velocity compared to the initial contact.

The distribution of the energy dissipation near the bubble is shown in figures 13 and 14. These figures show that the majority of the energy dissipation takes place at the rim of the lamella during the interaction and in the wake of the bubble after the collision has taken place. This suggests that the assumption of Heitkam et al. regarding energy dissipation at the rim of the lamella is correct, but dissipation inside the lamella itself can not be neglected.

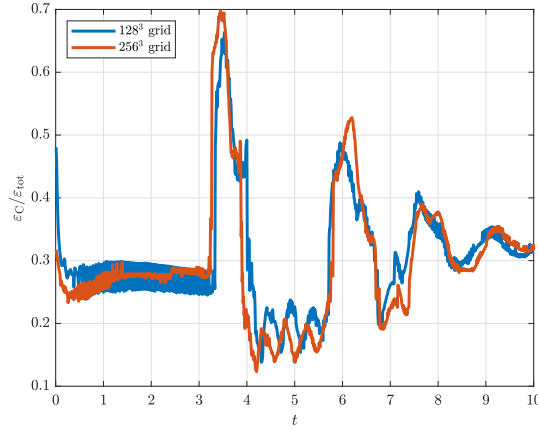


Figure 11: Energy dissipation in the control volume as a fraction of the total dissipation.

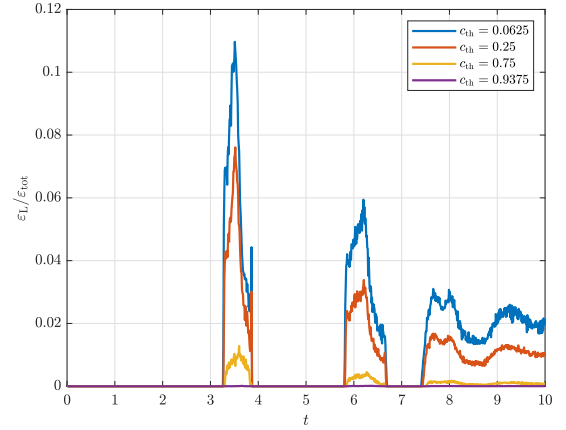


Figure 12: Energy dissipation in the lamella as a fraction of the total dissipation on the  $256^3$  grid, for different values of  $c_{th}$ .

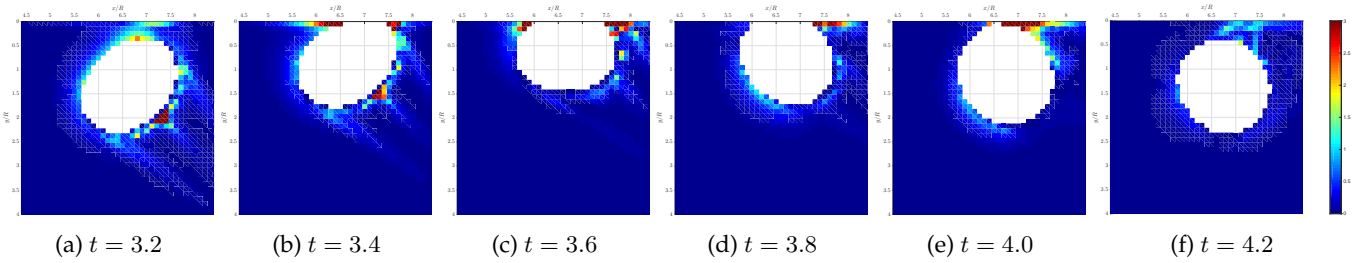


Figure 13: Energy dissipation in the vicinity of the bubble at different times on the  $128^3$  grid. Note that the bubble has been translated to the center of the domain to obtain a clearer picture. The values range from 0 (blue) to 3 (red), values beyond this range are clipped.

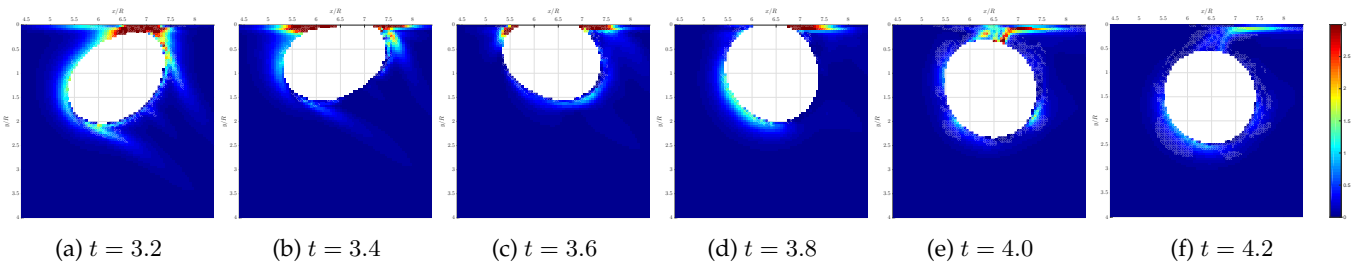


Figure 14: Energy dissipation in the vicinity of the bubble at different times on the  $256^3$  grid. The values range from 0 (blue) to 3 (red), values beyond this range are clipped.

The contact area  $R_a$  with the wall over time is shown in figure 15, where several values of  $c_{th}$  are considered. The dashed lines represent the contact area based on the corresponding value of  $c_{th}$  on the coarse grid. The different values of  $c_{th}$  yield the same behaviour, with a slight increase of the amplitude of  $R_a$  for smaller values of  $c_{th}$ . The relation between  $\Delta$  and  $R_a$ , shown in figure 16, is of more interest for comparison with the

reference paper. The proposed relation between  $\Delta$  and  $R_a$  is given by the dashed yellow line, which clearly does not agree with the results from the TBFsolver. The relation between the variables can be approximated by a square root function such as  $R_a/R = 1.25\sqrt{\Delta/R}$ , depicted by the dashed purple line. This function is chosen for illustrational purposes and is not assumed to be the best approximating function.

It is unclear the cause is of the discrepancy between the prediction of Heitkam et al. of the relation between  $\Delta$  and  $R_a$  and the actual results. It seems as if the cause is a scaling issue. However, this should not be the case since equation (7) gives the relation between the nondimensionalized quantities  $\Delta/R_a$  and  $R_a/R$ .

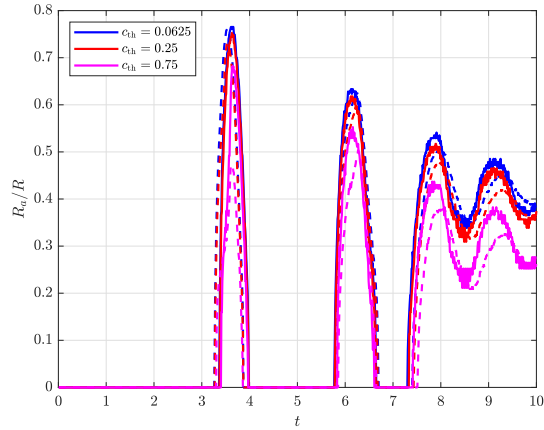


Figure 15: Contact area radius  $R_a$  for different values of  $c_{th}$ . The dashed lines represent the corresponding values of  $c_{th}$  on the  $128^3$  grid.

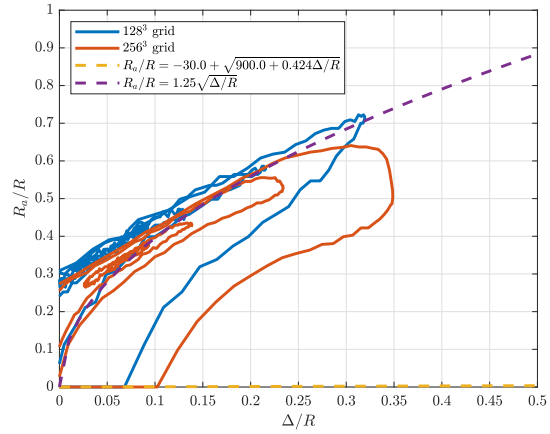


Figure 16: Relation between  $R_a/R$  and  $\Delta/R$ .

### 3.5 Results 0 degree case

The development of the center of mass and the velocity of the bubble is shown in figures 17 and 18. Similar to the results of the 45 degree case, the bubble rises slightly faster on the fine grid than on the coarse grid.

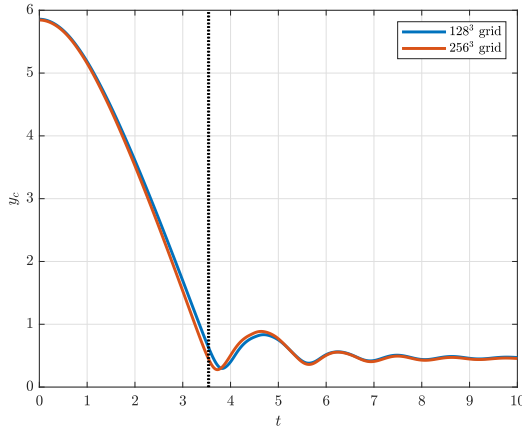


Figure 17:  $y$ -center of mass over time.

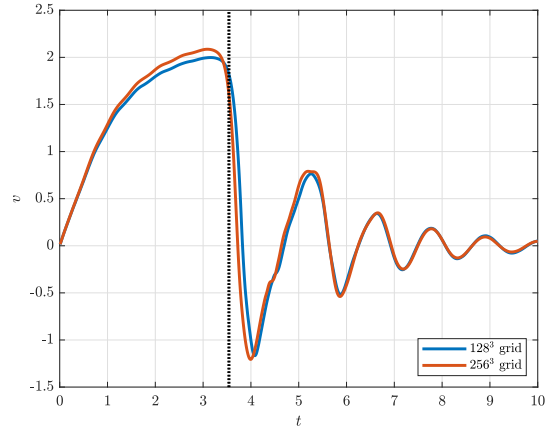


Figure 18: Velocity normal to the wall.

#### Comparison with the model assumptions

Figure 19 shows that the minimum distance between the bubble and the wall shows similar behaviour on both grids. The minimum distance during the collision process becomes smaller as the bubble Reynolds at the initial moment of the collision decreases. This is also observed when comparing these results to those of the 45 degree case (figure 9); the latter shows a smaller minimum distance at the first bubble-wall interaction.

A cross-section of the bubble shape near the wall is shown in figure 20. Note that the distance from the wall is expressed in the grid size of the  $256^3$  grid in this figure, as to clearly show the dimpled shape of the lamella and the change over time.

The differences in the total dissipation on both grids are best seen in the peaks that occur when the bubble hits the wall, as shown in figure 21. The dissipation before the initial collision is equal to that of the 45 degree case, which is to be expected since the bubble moves freely and at the same velocity this period. The peak in the energy dissipation is between almost twice as large compared to the 45 degree case. This is caused by the larger approach velocity of the bubble, which results in larger fluid displacement in the lamella, which in turn yields a larger energy dissipation rate during the collision.

This effect can also be observed in figures 23 and 24, which both show higher peaks during the initial collision than their 45 degree counterparts.

Figure 22 has been added for completeness and displays the relation between the dissipation in the lamella and the value of  $c_{th}$ . No clear way of determining which cells are part of the fluid lamella has been found, hence it is important to sketch how the threshold value  $c_{th}$  relates to the dissipation inside the lamella.

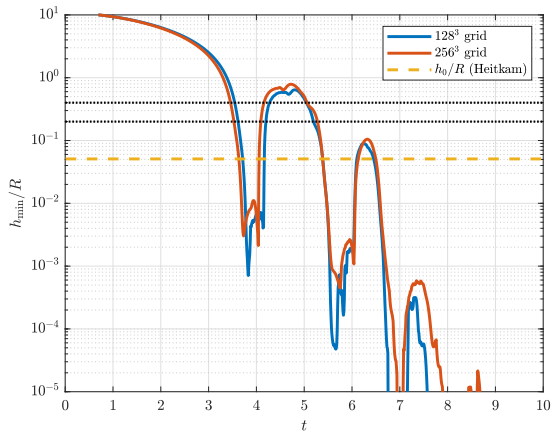


Figure 19: Minimum distance between the bubble and the wall.

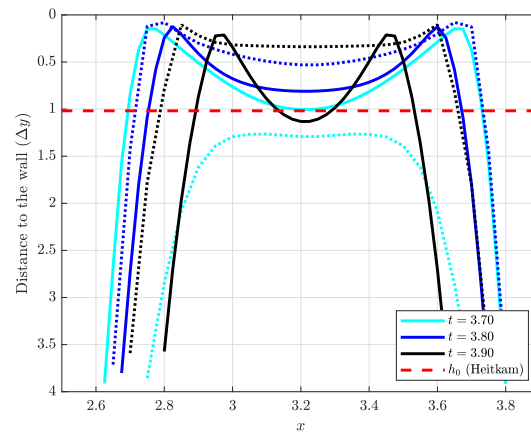


Figure 20: Shape of the bubble near the wall at different times. The dashed lines represent the results of  $128^3$  grid, the solid lines represent those of the  $256^3$  grid.

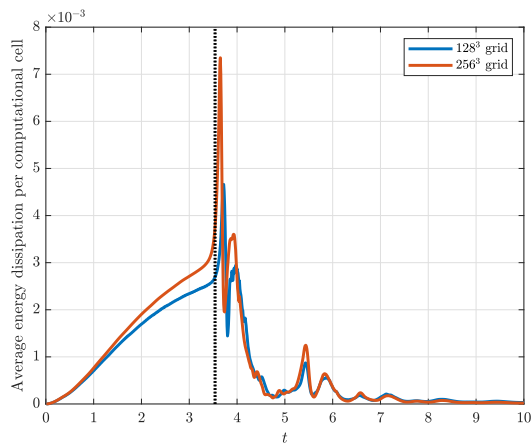


Figure 21: Energy dissipation in the entire fluid region.

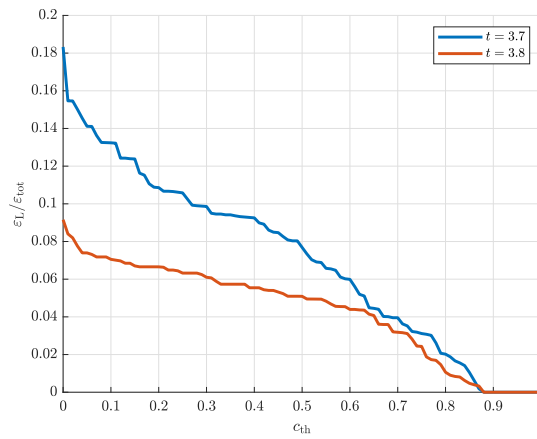


Figure 22: Energy dissipation in the lamella plotted against  $c_{th}$  at fixed times.

The distribution of the energy dissipation for the considered grids is given in figure 25 and 26. Energy dissipation is taking place in the lamella and at its rim, similar to the 45 degree case.

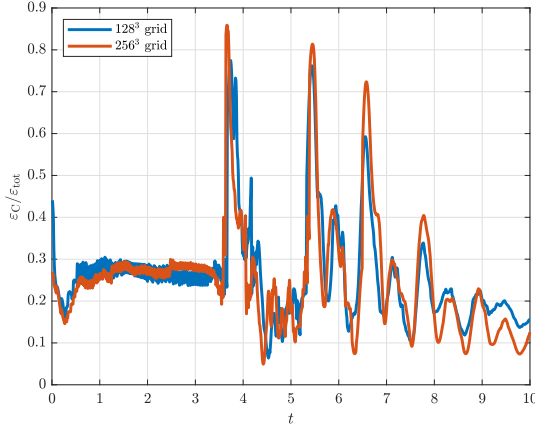


Figure 23: Energy dissipation in the control volume as a fraction of the total dissipation.

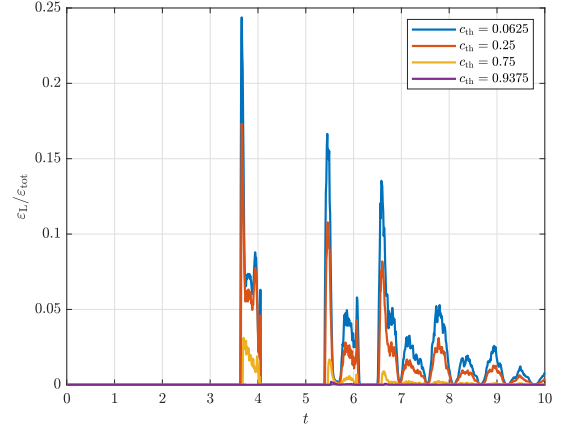


Figure 24: Energy dissipation in the lamella as a fraction of the total dissipation on the  $256^3$  grid, for different values of  $c_{th}$ .

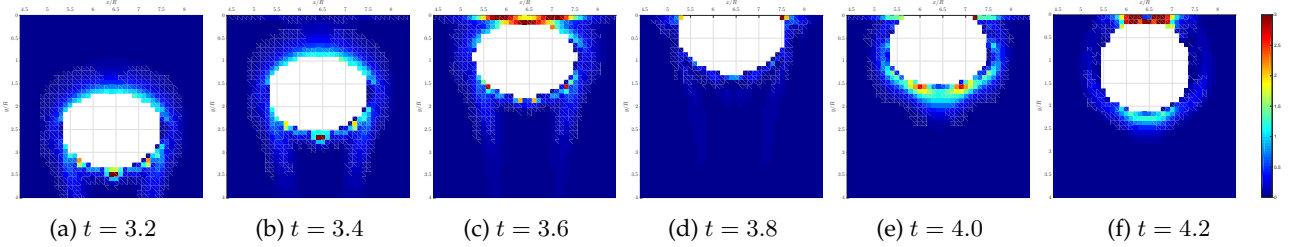


Figure 25: Energy dissipation in the vicinity of the bubble at different times on the  $128^3$  grid. The values range from 0 (blue) to 3 (red), values beyond this range are clipped.

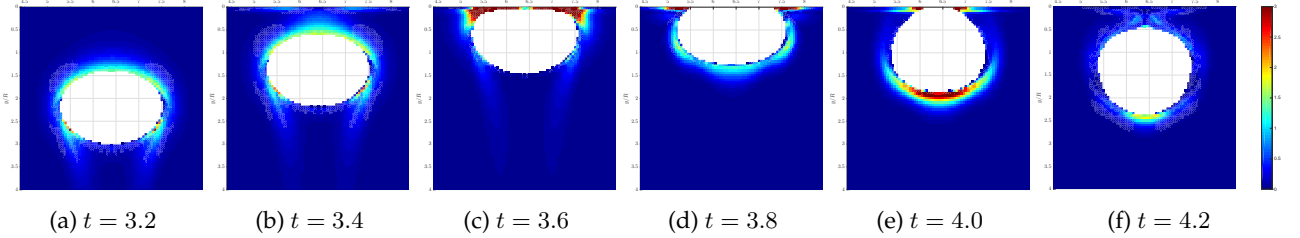


Figure 26: Energy dissipation in the vicinity of the bubble at different times on the  $256^3$  grid. The values range from 0 (blue) to 3 (red), values beyond this range are clipped.

The contact area with the wall for different values of  $c_{th}$  is shown in figure 27. The obtained values on the different grids are in good agreement, especially compared to the 45 degree case. It is assumed that the disagreement in the 45 degree case is caused by the tangential movement of the bubble, which results in a larger grid dependency.

As with the 45 degree case, the proposed relation between  $R_a$  and  $\Delta$  does not at all agree with the data obtained from the TBFsolver. This is depicted in figure 28. The line given by  $R_a/R = 1.25\sqrt{(\Delta/R)}$  is given in this figure as well, to provide an example relation that better describes

the results.

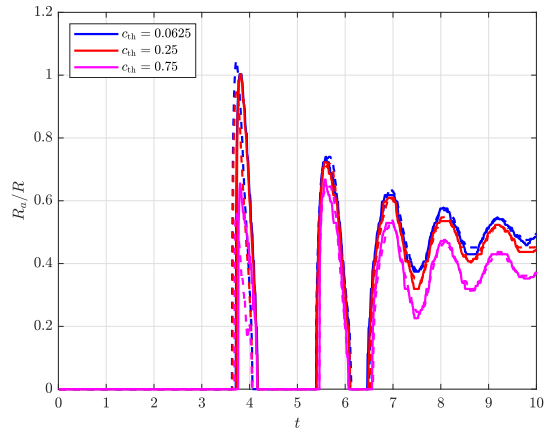


Figure 27: Contact area radius  $R_a$  for different values of  $c_{th}$ . The dashed lines represent the corresponding values of  $c_{th}$  on the  $128^3$  grid.

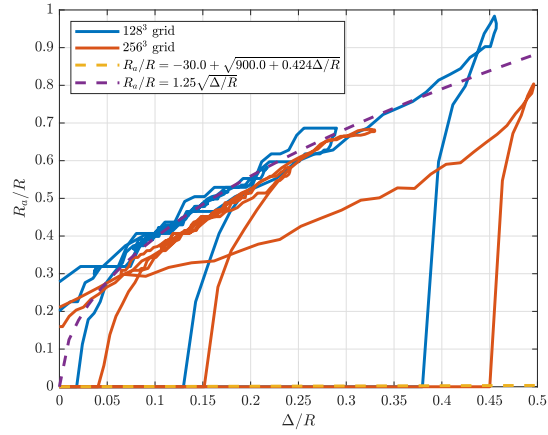


Figure 28: Relation between the contact area  $R_a/R$  and the deformation  $\Delta/R$ .

### 3.6 Concluding remarks

In this section several tests regarding bubble-wall interactions are performed. The parameters in these test were specifically chosen such that the results could be compared to those in made for the model proposed by Heitkam et al. and some of the assumptions could be tested.

With the obtained data of the TBFsolver, we found the following results:

- The bubble movement and velocity on the coarse and fine grids were in strong agreement, even after the initial bubble-wall interaction.
- The minimum distance between the bubble and the wall showed the same behaviour on the coarse and the fine grids, even for values smaller than the grid size. Moreover, the value of the minimum distance during the collision becomes smaller for small normal bubble velocity.
- The energy dissipation in the fluid significantly increases during the bubble-wall interaction. This effect is more pronounced for the 0 degree case than for the 45 degree case. The majority of the dissipation during the collision takes place in the control volume as defined earlier.

Regarding the assumptions made by Heitkam et al., we conclude the following:

- The lamella thickness is not constant during the collision. The average thickness is not determined, since it is unclear at what point the space between the bubble and the wall is actually considered as the lamella. However, the minimum distance between the bubble and the wall is not constant during the collision process.
- The variable lamella thickness during the bubble-wall interaction results in energy dissipation taking place there. It was found that up to ten percent of the total dissipation can

take place in the lamella for the 45 degree case, and up to twenty five percent for the 0 degree case.

- The proposed relation between the deformation of the bubble and the contact area with the wall does not at all agree with the obtained results. It is difficult to obtain an expression which can be labeled as the best fit, due to the unclear definition of the contact area.

---

## 4 Lubrication theory

The fluid film between the bubble and the wall possesses a useful property in the asymptotic aspect ratio between the wall-normal and the wall-tangential length scales. The difference in magnitude between these scales can be exploited to obtain an approximation of the Navier-Stokes equations, where viscosity is dominant [14]. The flow inside the fluid lamella can be reconstructed from these viscous flow equations. Lubrication theory describes the mathematics and analysis behind this approximation. Essential in this field is the Reynolds equation, which provides an expression for the pressure distribution.

Lubrication theory is traditionally used in many applications within mechanical engineering and is sometimes used for biomedical purposes as well. An example for the latter is the modeling of human joints, such as ankle joints [21]. Applications in mechanical engineering usually include lubrication for bearings. Oftentimes fixed shapes such as solid spheres (Davis et al. [8], Gu et al. [11], Goddard et al. [10]) or cylinders [22] are used, or the effects of surface roughness are included [3]. More general forms such as stated by Kundu et al. [14] often assume the flow is contained within two (nearly) parallel surfaces, which implies a negligible curvature. Simulation results in section 3 show that the curvature of the bubble interface at the lamella is clearly visible on the length scales of the lamella thickness and can therefore not be neglected.

This section deals with the derivation of the lubrication equations and the application of these equations to a bubble-wall interaction. This application requires the inclusion of the curvature. The Navier-Stokes equations are first simplified using the asymptotic aspect ratio of the length scales. Expressions for the velocity field are subsequently obtained, which in turn are used to achieve a description of the pressure distribution in the form of the Reynolds equation. The flow in the lamella can then be reconstructed by using a numerical approximation of the solution to the Reynolds equation.

This section is structured as follows. Nondimensionalization and simplification of the Navier-Stokes equations is described in sections 4.1 and 4.2, respectively. The general problem of finding the lubrication pressure is discussed in section 4.3 and a method for finding this pressure in a one-dimensional case is presented in section 4.4. This method is applied to explicitly defined bubble interfaces in section 4.5, to provide an example of a reconstructed flow for a given bubble interface. Subsequently, lubrication theory is applied to the results obtained in the previous section, this is shown in section 4.6. The possibilities of implementing lubrication theory in the TBFsolver are discussed in section 4.7. Concluding remarks are collected in section 4.8.

### 4.1 Nondimensionalization of the Navier-Stokes equations

#### Equations and scalings

The continuity equation and Navier-Stokes equations for incompressible flows form the starting point for the analysis. These equations are given by

$$\nabla \cdot \mathbf{u} = 0, \tag{8}$$

$$\rho \left( \frac{\partial \mathbf{u}}{\partial t} + \mathbf{u} \cdot \nabla \mathbf{u} \right) = -\nabla p + \mu \nabla^2 \mathbf{u} + \rho \mathbf{g}. \tag{9}$$

We fully write down these equations, because the scalings are dependent on the direction under consideration:

$$\frac{\partial u}{\partial x} + \frac{\partial v}{\partial y} + \frac{\partial w}{\partial z} = 0, \quad (10)$$

$$\rho \left( \frac{\partial u}{\partial t} + u \frac{\partial u}{\partial x} + v \frac{\partial u}{\partial y} + w \frac{\partial u}{\partial z} \right) = -\frac{\partial p}{\partial x} + \mu \left( \frac{\partial^2 u}{\partial x^2} + \frac{\partial^2 u}{\partial y^2} + \frac{\partial^2 u}{\partial z^2} \right), \quad (11)$$

$$\rho \left( \frac{\partial v}{\partial t} + u \frac{\partial v}{\partial x} + v \frac{\partial v}{\partial y} + w \frac{\partial v}{\partial z} \right) = -\frac{\partial p}{\partial y} + \mu \left( \frac{\partial^2 v}{\partial x^2} + \frac{\partial^2 v}{\partial y^2} + \frac{\partial^2 v}{\partial z^2} \right), \quad (12)$$

$$\rho \left( \frac{\partial w}{\partial t} + u \frac{\partial w}{\partial x} + v \frac{\partial w}{\partial y} + w \frac{\partial w}{\partial z} \right) = -\frac{\partial p}{\partial z} + \mu \left( \frac{\partial^2 w}{\partial x^2} + \frac{\partial^2 w}{\partial y^2} + \frac{\partial^2 w}{\partial z^2} \right). \quad (13)$$

Using the scalings

$$\begin{aligned} x &= R\tilde{x}, & y &= R\tilde{y}, & z &= H_0\tilde{z}, \\ u &= U\tilde{u}, & v &= U\tilde{v}, & w &= W\tilde{w}, \\ \nabla &= R\tilde{\nabla}, & t &= (R/U)\tilde{t}, & p &= (\mu UR/H_0^2)\tilde{p}. \end{aligned}$$

Here  $R$  is the bubble radius,  $H_0$  is the distance between the bubble interface and the wall.  $U$  denotes the flow velocity tangent to the wall, whereas  $W$  denotes the flow velocity normal to the wall. We omit the tildes from now on.

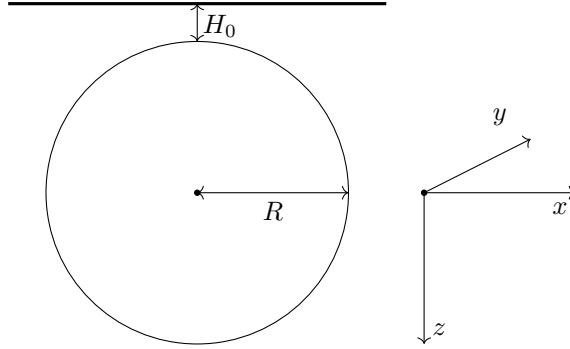


Figure 29: Sketch of the geometry.

### Nondimensional form

Starting with the continuity equation, we obtain

$$\frac{U}{R} \left( \frac{\partial u}{\partial x} + \frac{\partial v}{\partial y} \right) + \frac{W}{H_0} \frac{\partial w}{\partial z} = 0. \quad (14)$$

Adding a term  $(U/R)\partial w/\partial z$  allows us to substitute equation (10) into (14). Subsequently subtracting the same term to keep the equation correct yields  $U = W \frac{R}{H_0}$ , this is based on Manica et al. [18].

Using the film Reynolds number  $\text{Re}_f = (\rho H_0 W)/\mu$  we obtain the nondimensionalized Navier-Stokes equations, given by

$$\text{Re}_f \left( \frac{\partial u}{\partial t} + u \frac{\partial u}{\partial x} + v \frac{\partial u}{\partial y} + w \frac{\partial u}{\partial z} \right) = -\frac{\partial p}{\partial x} + \frac{H_0^2}{R^2} \left( \frac{\partial^2 u}{\partial x^2} + \frac{\partial^2 u}{\partial y^2} \right) + \frac{\partial^2 u}{\partial z^2}, \quad (15)$$

$$\text{Re}_f \left( \frac{\partial v}{\partial t} + u \frac{\partial v}{\partial x} + v \frac{\partial v}{\partial y} + w \frac{\partial v}{\partial z} \right) = -\frac{\partial p}{\partial y} + \frac{H_0^2}{R^2} \left( \frac{\partial^2 v}{\partial x^2} + \frac{\partial^2 v}{\partial y^2} \right) + \frac{\partial^2 v}{\partial z^2}, \quad (16)$$

$$\text{Re}_f \left( \frac{\partial w}{\partial t} + u \frac{\partial w}{\partial x} + v \frac{\partial w}{\partial y} + w \frac{\partial w}{\partial z} \right) = -\frac{R^2}{H_0^2} \frac{\partial p}{\partial z} + \frac{H_0^2}{R^2} \left( \frac{\partial^2 w}{\partial x^2} + \frac{\partial^2 w}{\partial y^2} \right) + \frac{\partial^2 w}{\partial z^2}. \quad (17)$$

## 4.2 Simplification of nondimensionalised Navier-Stokes equations

We are only interested in the situation where the bubble is near the wall, that is, when  $H_0/R$  is small. Neglecting the terms  $H_0/R$  yields

$$\text{Re}_f \left( \frac{\partial u}{\partial t} + u \frac{\partial u}{\partial x} + v \frac{\partial u}{\partial y} + w \frac{\partial u}{\partial z} \right) = -\frac{\partial p}{\partial x} + \frac{\partial^2 u}{\partial z^2}, \quad (18)$$

$$\text{Re}_f \left( \frac{\partial v}{\partial t} + u \frac{\partial v}{\partial x} + v \frac{\partial v}{\partial y} + w \frac{\partial v}{\partial z} \right) = -\frac{\partial p}{\partial y} + \frac{\partial^2 v}{\partial z^2}, \quad (19)$$

$$\frac{\partial p}{\partial z} = 0. \quad (20)$$

Recall that  $\text{Re}_f = \rho W H_0/\mu$  and  $U H_0 = W R$  and therefore  $\text{Re}_f$  is small too, which in turn results in

$$\frac{\partial p}{\partial x} = \frac{\partial^2 u}{\partial z^2}, \quad (21)$$

$$\frac{\partial p}{\partial y} = \frac{\partial^2 v}{\partial z^2}, \quad (22)$$

$$\frac{\partial p}{\partial z} = 0. \quad (23)$$

All variables up to this point have been scaled, scaling back to the original variables gives us the following equations. Keep in mind that these involve the 'physical' variables:

$$\frac{\partial p}{\partial x} = \mu \frac{\partial^2 u}{\partial z^2}, \quad (24)$$

$$\frac{\partial p}{\partial y} = \mu \frac{\partial^2 v}{\partial z^2}, \quad (25)$$

$$\frac{\partial p}{\partial z} = 0. \quad (26)$$

### Flow inside the fluid film

Assume a bubble-wall interaction, with velocity  $\mathbf{u}_g = (u_g, v_g, w_g)$  at the bubble interface. We can without loss of generality assume that the wall is stationary. Moreover,  $h(x, y)$  denotes the

distance between the bubble and the wall at  $(x, y)$ , where we take  $z = 0$  at the wall. Integrating the equations above and applying the boundary conditions gives us

$$u(x, y, z) = \frac{1}{2\mu} \frac{\partial p}{\partial x} (z^2 - h(x, y)z) + \frac{u_g}{h(x, y)} z, \quad (27)$$

$$v(x, y, z) = \frac{1}{2\mu} \frac{\partial p}{\partial y} (z^2 - h(x, y)z) + \frac{v_g}{h(x, y)} z. \quad (28)$$

The expression for  $w$  follows from equations (27) and (28) and the continuity equation. For this reason the desired partial derivatives of  $u$  and  $v$  are calculated as

$$\frac{\partial u}{\partial x} = \frac{1}{2\mu} \frac{\partial^2 p}{\partial x^2} (z^2 - hz) - \frac{1}{2\mu} \frac{\partial p}{\partial x} \frac{\partial h}{\partial x} z - \frac{\partial h}{\partial x} \frac{u_g}{h^2} z, \quad (29)$$

$$\frac{\partial v}{\partial y} = \frac{1}{2\mu} \frac{\partial^2 p}{\partial y^2} (z^2 - hz) - \frac{1}{2\mu} \frac{\partial p}{\partial y} \frac{\partial h}{\partial y} z - \frac{\partial h}{\partial y} \frac{v_g}{h^2} z. \quad (30)$$

Inserting these results into the continuity equation yields an expression for  $\partial w / \partial z$ . Integrating over  $z$  and applying the boundary condition  $w|_{z=0} = 0$  gives

$$w(x, y, z) = -\frac{1}{6\mu} \left( \frac{\partial^2 p}{\partial x^2} + \frac{\partial^2 p}{\partial y^2} \right) z^3 + \frac{1}{4\mu} \left( \frac{\partial}{\partial x} \left[ h \frac{\partial p}{\partial x} \right] + \frac{\partial}{\partial y} \left[ h \frac{\partial p}{\partial y} \right] \right) z^2 + \frac{1}{2} \left( \frac{\partial h}{\partial x} \frac{u_g}{h^2} + \frac{\partial h}{\partial y} \frac{v_g}{h^2} \right) z^2. \quad (31)$$

### Fluid film evolution and wall-normal velocity in the case of negligible curvature

Equation (31) can be simplified when we assume the local fluid film thickness variation is small. This assumption means  $\partial h / \partial x$  and  $\partial h / \partial y$  are small, i.e., that the curvature of the bubble interface is small, which reduces the equation to

$$w(x, y, z) = -\frac{1}{6\mu} \left( \frac{\partial^2 p}{\partial x^2} + \frac{\partial^2 p}{\partial y^2} \right) z^3 + \frac{h}{4\mu} \left( \frac{\partial^2 p}{\partial x^2} + \frac{\partial^2 p}{\partial y^2} \right) z^2. \quad (32)$$

Applying the boundary condition  $w|_{z=h} = \partial h / \partial t$  gives

$$\frac{\partial h}{\partial t} = \frac{h^3}{12\mu} \left( \frac{\partial^2 p}{\partial x^2} + \frac{\partial^2 p}{\partial y^2} \right). \quad (33)$$

Equation (33) allows us to express the wall-normal velocity in terms of the approach speed of the bubble. For this purpose we define  $\alpha(x, y, z) := z/h(x, y)$ , which will simply denoted by  $\alpha$ , and write

$$w(\alpha) = \frac{h^3}{12\mu} \frac{\partial^2 p}{\partial x^2} (3\alpha^2 - 2\alpha^3) = \frac{\partial h}{\partial t} (3\alpha^2 - 2\alpha^3). \quad (34)$$

This expression agrees with the boundary condition  $w|_{z=h/2} = d(h/2)/dt$  [23].

### Fluid film evolution and wall-normal velocity

A more general form of equation (33) can be obtained by realizing that the change in volume occupied by the bubble plus the change in volume occupied by the liquid should equal zero

in the area near the wall. The change of volume occupied by the bubble can be expressed by the movement of the interface,  $\partial h/\partial t$ . The change of volume occupied by the fluid equals the outflow over the boundaries of the domain. This is mathematically expressed as

$$\int_x \int_y \frac{\partial h}{\partial t} dy dx + \int_x \int_y \int_z \frac{\partial u}{\partial x} + \frac{\partial v}{\partial y} dz dy dx = 0, \quad (35)$$

where the last volume integral resulted from the divergence theorem. In turn, this yields

$$\frac{\partial h}{\partial t} + \int_0^{h(x,y)} \frac{\partial u}{\partial x} dz + \int_0^{h(x,y)} \frac{\partial v}{\partial y} dz = 0. \quad (36)$$

The two integrals can be rewritten using Leibniz's rule:

$$\int_{a(x)}^{b(x)} \frac{\partial}{\partial x} f(x, t) dt = \frac{d}{dx} \left( \int_{a(x)}^{b(x)} f(x, t) dt \right) - f(x, b(x)) \cdot \frac{d}{dx} b(x) + f(x, a(x)) \cdot \frac{d}{dx} a(x), \quad (37)$$

after which we obtain

$$\frac{\partial h}{\partial t} + \frac{\partial}{\partial x} \left( \int_0^{h(x,y)} u dz \right) + \frac{\partial}{\partial y} \left( \int_0^{h(x,y)} v dz \right) - u_g \frac{\partial h}{\partial x} - v_g \frac{\partial h}{\partial y} = 0. \quad (38)$$

The integrals can be evaluated by simply using the expressions for  $u$ , equation (27), and  $v$ , equation (28), as found before:

$$\int_0^{h(x,y)} u dz = -\frac{1}{12\mu} \frac{\partial p}{\partial x} h(x, y)^3 + \frac{1}{2} u_g h(x, y), \quad (39)$$

$$\int_0^{h(x,y)} v dz = -\frac{1}{12\mu} \frac{\partial p}{\partial y} h(x, y)^3 + \frac{1}{2} v_g h(x, y). \quad (40)$$

Now the derivatives of these integrals are calculated and are given by

$$\frac{\partial}{\partial x} \int_0^{h(x,y)} u dz = -\frac{1}{12\mu} \left( \frac{\partial^2 p}{\partial x^2} h(x, y)^3 + 3 \frac{\partial p}{\partial x} h(x, y)^2 \frac{\partial h}{\partial x} \right) + \frac{1}{2} u_g \frac{\partial h}{\partial x}, \quad (41)$$

$$\frac{\partial}{\partial y} \int_0^{h(x,y)} v dz = -\frac{1}{12\mu} \left( \frac{\partial^2 p}{\partial y^2} h(x, y)^3 + 3 \frac{\partial p}{\partial y} h(x, y)^2 \frac{\partial h}{\partial y} \right) + \frac{1}{2} v_g \frac{\partial h}{\partial y}. \quad (42)$$

We substitute these terms into (38) and rewrite the formulation to obtain a partial differential equation for  $h$ . Note that  $h(x, y)$  is simply written as  $h$  for the sake of readability. The equation is given by

$$\frac{\partial h}{\partial t} + \frac{\partial h}{\partial x} \left( -\frac{1}{4\mu} \frac{\partial p}{\partial x} h^2 - \frac{1}{2} u_g \right) + \frac{\partial h}{\partial y} \left( -\frac{1}{4\mu} \frac{\partial p}{\partial y} h^2 - \frac{1}{2} v_g \right) - \frac{h^3}{12\mu} \left( \frac{\partial^2 p}{\partial x^2} + \frac{\partial^2 p}{\partial y^2} \right) = 0. \quad (43)$$

When  $\frac{\partial h}{\partial t} = w_g$ , which is the case when the approach volume of the interface equals the wall-normal velocity of the bubble, the Reynolds equation for constant density is obtained:

$$\frac{\partial}{\partial x} \left( \frac{h^3}{12\mu} \frac{\partial p}{\partial x} \right) + \frac{\partial}{\partial y} \left( \frac{h^3}{12\mu} \frac{\partial p}{\partial y} \right) = w_g - \frac{u_g}{2} \frac{\partial h}{\partial x} - \frac{v_g}{2} \frac{\partial h}{\partial y}. \quad (44)$$

### 4.3 Finding the lubrication pressure

Finding the pressure in the gap between the bubble and the wall, the lubrication pressure, is the main problem of interest. This pressure can be used to either find the velocity profile in the gap using equations (27), (28) and (32), or to derive a certain resistance force that acts on the interface of the bubble similar to Zhang and Law [23].

Assume  $\partial h/\partial t$  and  $h$  are known. Then either the Poisson equation (33) can be solved for  $p$  when the curvature is assumed to be small, or a solution to the Reynolds equation (44) can be found when the curvature is to be included. The advantage of using the Poisson equation (33) is that finding an analytic solution might be easier. However, neglecting the curvature effects only leads to accurate solutions in a limited number of situations.

Below it is argued that the Reynolds equation should be used for finding the pressure in the gap. Solving this equation can be done using regular methods for solving discrete Poisson equations, such as multigrid methods or methods involving the fast Fourier transform.

#### Domain and boundary conditions

The natural question that arises is what boundary conditions should be applied for the pressure. This depends on the domain in which the equation is solved. A pressure difference between the bubble and the liquid exists when the curvature of the interface is nonzero, as stated by the Young-Laplace equation. It would therefore be sensible to define a rectangular or square area around the bubble where the equation should be solved. A rectangular shape matches the spatial discretization used in the TBFsolver and can be chosen such that it encompasses all cells near the boundary for which  $0 < c < 1$  for the volume fraction.

The edges of the rectangular domain could consist of cells with a small value of  $c$ , i.e., the value of  $h$  is relatively large in these cells. This results in a small value of the lubrication pressure. In other words, at the edges of the domain it can be assumed that  $p = 0$ . This choice coincides with that of Skotheim and Mahadevan [22].

#### Incorporating $\mathbf{u}_g$

Since we are interested in the velocity of the bubble interface in  $x$ ,  $y$ , and  $z$  directions, it would be logical to use the change in the volume fraction field for this case rather than the velocity field. Moreover, the volume fraction field is advected before the velocity in the current time step is calculated and the advected volume fraction field is used for calculating the velocity.

An intuitive approach would be to define  $\mathbf{u}_g$  based on the change of the center of mass of the bubble. This approach basically states that  $\partial h/\partial t$  can be replaced by  $w_g$ , which turns equation (43) into the Reynolds equation. While this would likely work for the velocities tangential to the wall, it would not always be accurate for the velocity normal to the wall due to the bubble deformation. A possible solution to this would be to use the change in the center of mass of the volume fraction field in one or a few layers of cells adjacent to the wall, which would also more accurately represent the bubble movement near the wall.

#### 4.4 Lubrication pressure in one-dimension

We will now consider equation (44) reduced to one dimension with no movement tangential to the wall. After fully writing the derivative we obtain

$$\frac{h^3}{12\mu} \frac{d^2 p}{dx^2} + \frac{1}{4\mu} \frac{dh}{dx} h^2 \frac{dp}{dx} = w_g. \quad (45)$$

For now it is assumed that the wall-normal velocity is equal for the entire bubble, which means  $w_g$  is independent of  $x$ .

##### Analytic solution

When we define  $f(x) := \frac{h^3}{12\mu}$  and  $g(x) := \frac{w_g}{f(x)}$ , the equation as shown below is obtained. The notation of  $\frac{d}{dx}$  is replaced by a prime  $'$  for readability, yielding

$$p''(x) + \frac{f'(x)}{f(x)} p'(x) = g(x). \quad (46)$$

From this point the following method for solving nonhomogeneous second order differential equations with non-constant coefficients is employed.

1. Substitute  $q(x)$  for  $p'(x)$  to obtain a first order differential equation.
2. Calculate the integrating factor  $\gamma(x) = \exp\left(\int \frac{f'(x)}{f(x)} dx\right)$ .
3. Calculate  $q(x) = \frac{\int \gamma(x)g(x) dx}{\gamma(x)}$ .
4. Integrate  $q(x)$  to obtain  $p(x) = \int q(x) dx$ .

Applying step 1 is straightforward and is not explicitly shown. The derivation of  $\gamma(x)$  for step 2 yields

$$\gamma(x) = \exp\left(\int \frac{f'(x)}{f(x)} dx\right) = \exp\left(3 \int \frac{h'(x)}{h(x)} dx\right) = \exp(3 [\log(h(x)) + \tilde{c}_1]) = c_1 h^3(x), \quad (47)$$

where  $c_1$  is a constant. Recall that  $g(x) = w_g/f(x) = 12w_g\mu/h^3(x)$  and therefore we obtain  $q(x)$  as

$$q(x) = \frac{\int \gamma(x)g(x) dx}{\gamma(x)} = \frac{\int 12c_1 w_g \mu dx}{c_1 h^3(x)} = \frac{12w_g \mu x + \tilde{c}_2}{h^3(x)}. \quad (48)$$

Finally, the pressure results from applying step 4,

$$p(x) = \int q(x) dx = 12w_g \mu \int \frac{x + c_2}{h^3(x)} dx. \quad (49)$$

Unfortunately,  $h(x)$  is usually not known and if it is known, the term  $h^3(x)$  would likely be very complex and impractical to work with. Equation (49) does provide some information about the pressure distribution in the one-dimensional case, namely:

- The pressure scales linearly with the approach speed  $w_g$  and the viscosity  $\mu$ .
- The integral term on the right hand side of equation (49) becomes small when  $h(x)$  is large and becomes large when  $h(x)$  is small, corresponding to a high pressure in places where the bubble is close to the wall.

## Numerical method

Since the analytic solution can generally not be further evaluated than the form in (49), a numerical solution is used to investigate the behaviour of the function.

The domain on which the function is solved is  $[0, 1]$ . The problem can be seen as axisymmetrical when the boundary conditions of  $p$  and  $h$  are chosen properly. For this reason the left boundary, at  $x = 0$ , requires  $p'(x) = 0$  and  $h'(x) = 0$ , which corresponds to  $x = 0$  being the radial center of the bubble interface. The lubrication pressure is assumed to be zero at  $x = 1$ , which is the case when the distance between the bubble and the wall is large.

A Gauss-Seidel solver is used to iteratively approximate equation (45). The domain is divided into  $N$  intervals, with  $N + 1$  interval boundaries at which the pressure will be calculated. The distance between the bubble and the wall  $h(x)$  and the spatial derivatives of  $h(x)$  and  $p(x)$  are also defined on the interval boundaries. The derivatives are calculated using a standard central finite difference scheme.

Given the approximated solution at iteration  $k$  and at interval boundaries 1 to  $i - 1$ , the solution at iteration  $k + 1$  at interval boundary  $i$  can be calculated. Subsequently the solution at iteration  $k + 1$  is calculated at interval boundary  $i + 1$ , and so on until a solution has been calculated on the entire domain at iteration  $k + 1$ . Applying this algorithm for the entire domain is called a sweep. Note that the superscripts  $k$  and  $k + 1$  denote the iteration number, the other superscripts denote a power. The scheme is given by

$$f_i^k = \frac{12\mu v g}{h_i^3} - 3 \left( \frac{dh}{dx} \right)_i \left( \frac{dp}{dx} \right)_i \frac{1}{h_i}, \quad (50)$$

$$Lp_i^k = \frac{p_{i+1}^k - 2p_i^k + p_{i-1}^{k+1}}{(\Delta x)^2}, \quad (51)$$

$$r_i^k = f_i^k - Lp_i^k, \quad (52)$$

$$d_i^k = \frac{-(\Delta x)^2 r_i^k}{2}, \quad (53)$$

$$p_i^{k+1} = p_i^k + d_i^k. \quad (54)$$

In order to properly incorporate the boundary condition  $p(1) = 0$ , the interface shape  $h(x)$  is defined using the desired shape for  $x \leq x_s$ . Here  $0 < x_s < 1$  has a chosen value. Using a Dirichlet boundary condition rather than a Neumann boundary condition on the right boundary is also desirable since applying the latter on both boundaries results in a non-unique solution. This is the consequence of the term  $c_2$  in the integral in equation (49). The actual value of the pressure at the right boundary is dependent on the ambient pressure, but can be assumed to be zero without loss of generality.

An ellipsoidal shape is chosen for  $x > x_s$  as  $h(x)$  should be large at the right boundary. This shape is desirable since the value of  $h(1)$  can be varied easily and an appropriate choice of  $h(x)$  will lead to a continuous derivative  $h'(x)$ .

The numerical scheme (50-54) suffers from instabilities when curvature is present in the interface shape and  $n_x$  is not sufficiently large at the same time. This is most likely caused by inaccurate values of  $h'(x)$  when  $n_x$  is small, since no instabilities occur when  $h(x)$  is constant. In general, no instabilities have been found when  $n_x \geq 100$ .

The introduction of  $x_s$  grants us the opportunity to circumvent this problem. By defining  $h(x)$  and choosing  $x_s$  such that the desired shape is obtained within the interval  $[0, x_s]$  makes it possible to approximate the desired shape with less cells than  $n_x$  and still retain numerical stability.

### Validation of the numerical method

The numerical scheme (50-54) is validated by comparing the outcomes to the analytic solution (49). For this purpose we take  $h(x) = h_{\min}$  constant over the entire domain and fix  $\mu$  at 1 and  $w_g$  at  $-1$ , the latter means an approach velocity of 1. The pressure is then easily calculated and after applying the boundary conditions  $p'(0) = 0$  and  $p(1) = 0$  becomes  $p(x) = 6(1 - x^2)/h_{\min}^3$ .

The domain is divided into 150 equally sized intervals for this particular case and a total of  $2.5 \times 10^5$  Gauss-Seidel sweeps are performed for each value of  $h_{\min}$ . The results using  $h_{\min} = 1$  are shown in figure 30. It clearly shows that the numerically calculated pressure distribution approximates the analytical solution well, and consequently the derivative of the pressure.

Figure 31 shows the maximum value of the pressure for different values of  $h_{\min}$ . The numerical results coincide with the analytic solution, which indicates that the algorithm works as desired.

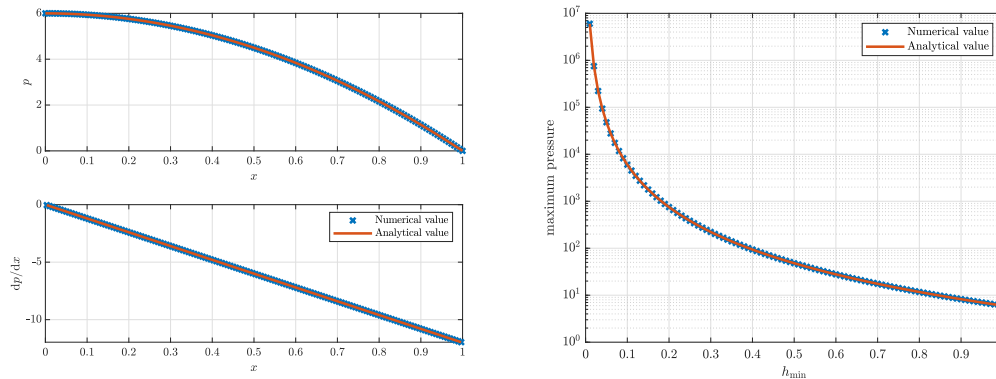


Figure 30: Pressure and first spatial derivative for  $h_{\min} = 1$ . Figure 31: Numerical and analytic maximum pressure values for different values of  $h_{\min}$ .

### Reconstruction of the flow velocity in the lamella

Given a pressure distribution for the axisymmetrical case, the flow in the lamella can be reconstructed using the one-dimensional counterpart of equations (27) and (31):

$$u(x, z) = \frac{1}{2\mu} p'(x) (z^2 - h(x)z), \quad (55)$$

$$w(x, z) = -\frac{1}{6\mu} p''(x) z^3 + \frac{1}{4\mu} (h'(x)p'(x) + h(x)p''(x)) z^2. \quad (56)$$

A uniform two-dimensional grid is used in order to recreate the flow. The flow values  $u$  and  $w$  as well as their spatial derivatives in both the  $x$ -direction and the  $z$ -direction are defined at the cell centers. This is possible because the function  $h(x)$  is known and can therefore easily be computed on the cell centers and the cell faces. The same holds for  $p(x)$  as it is obtained on the cell faces and thus the cell-centered values follow by interpolating. The functions  $h(x)$  and  $p(x)$  are independent of  $z$  and can hence be trivially extended into the  $z$ -direction. These properties allow  $u$  and  $v$  to be defined on the cell faces in the  $x$ -direction and  $z$ -direction and to subsequently calculate the derivatives at the cell centers using finite differences.

The availability of the derivatives at the cell centers allows us to calculate the energy dissipation at these positions. Since the coordinate system is cylindrical rather than Cartesian, the definition for the energy dissipation is slightly changed and is given by

$$\varepsilon = 2\frac{\mu}{\rho}S_{ij}^2, \quad \text{where}$$

$$S_{ij}^2 = \left(\frac{\partial u}{\partial x}\right)^2 + \left(\frac{u}{x}\right)^2 + \left(\frac{\partial w}{\partial z}\right)^2 + \frac{1}{4}\left(\frac{\partial u}{\partial z} + \frac{\partial w}{\partial x}\right)^2. \quad (57)$$

## 4.5 Application to explicitly defined interfaces

### Numerical setup

We again employ the numerical scheme (50-54) on the domain  $[0, 1]$ . The required input parameters for the algorithm are the interface shape  $h(x)$ , the approach speed  $w_g$ , the number of cells in the  $x$ -direction  $n_x$  and the fluid viscosity  $\mu$ . The number of cells in the  $z$ -direction  $n_z$  is not used for obtaining the pressure, but is only required for reconstructing the velocity field.

Two lamella interface shapes are considered, namely a straight interface and dimpled interface. Note that the dimpled shape given in equation (59) is chosen since it was easy to implement and roughly captures the typical shape of a lamella. The equations that were used to obtain the shapes are given by

$$h(x) = \begin{cases} h_{\min} & 0 \leq x \leq x_s \\ h_{\min} + b + h_{\text{ell}} - \frac{b+h_{\text{ell}}}{b}\sqrt{b^2 - (x - x_s)^2} & x_s \leq x \leq 1 \end{cases} \quad (58)$$

$$h(x) = \begin{cases} h_{\min} - \left(h_{\text{dim}} + h_{\text{dim}} \cos \frac{\pi x}{x_s}\right) & 0 \leq x \leq x_s \\ h_{\min} + b + h_{\text{ell}} - \frac{b+h_{\text{ell}}}{b}\sqrt{b^2 - (x - x_s)^2} & x_s \leq x \leq 1 \end{cases} \quad (59)$$

Equations (58) and (59) describe the straight interface shape and the dimpled interface shape, respectively, both with an ellipsoidal form for  $x \geq x_s$ . Here we used the notation  $b = 1 - x_s$  and denoted by  $h_{\text{ell}}$  the height of the ellipse. The variable  $x_{\text{dim}}$  denotes the center of the dimple,  $L_{\text{dim}}$  denotes its width and  $h_{\text{dim}}$  is the height of the dimple. A sketch of the dimpled shape and an explanation of the parameters is given in figure 32. We denote the number of sweeps of the algorithm by  $n_{\text{sweeps}}$ . The used values for the mentioned parameters are given in table 4.

Table 4: Parameters used for the comparison of the flow for different interface shapes.

$n_x$	$x_s$	$h_{\min}$	$h_{\text{ell}}$	$h_{\text{dim}}$	$x_{\text{dim}}$	$L_{\text{dim}}$	$n_{\text{sweeps}}$
200	0.2	$10^{-2}$	1	$5 \times 10^{-3}$	0	0.4	$1.25 \times 10^5$

## Results

The results for the straight and dimpled shapes are shown in figures 35 to 38. Note that a negative value of the velocity in  $z$ -direction means that the flow moves towards the wall, a positive

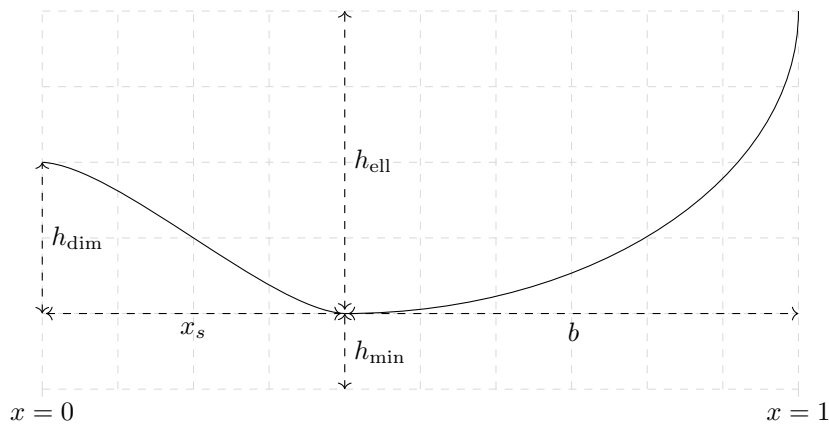


Figure 32: Sketch of the variables in the dimpled interface shape.

value means it is moving away from the wall.

Figures 33 and 34 show the pressure distribution and the derivative of the pressure, respectively. The straight shape and the dimpled shape show the same results for  $x \geq x_s$ , which is to be expected since the interfaces are equal on the interval  $[x_s, 1]$  and have the same boundary condition at  $x = 1$ . The dimpled shape results in a smaller pressure at  $x \leq x_s$  than the straight shape, caused by the larger distance between the interface and the wall. The figures clearly indicate that the straight shape coincides with a quadratic pressure distribution, which is in agreement with the analytic solution in equation (49).

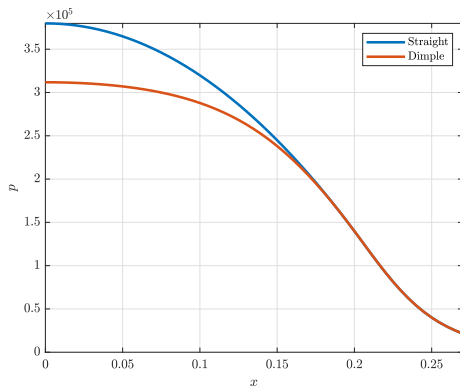


Figure 33: Pressure distributions.

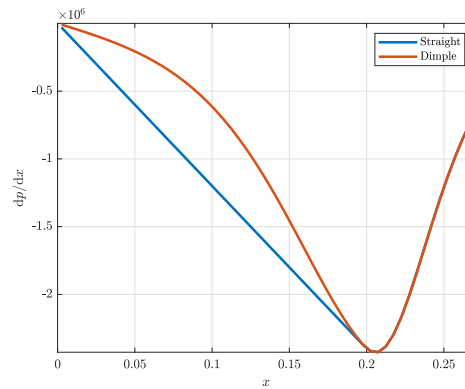


Figure 34: Pressure derivatives.

The parabolic flow profile of the velocity in  $x$ -direction is clearly visible for both cases in figures 35 and 36. The maximum wall-tangential velocity is obtained in halfway between the wall and the bubble interface at the point where the pressure gradient has its absolute maximum.

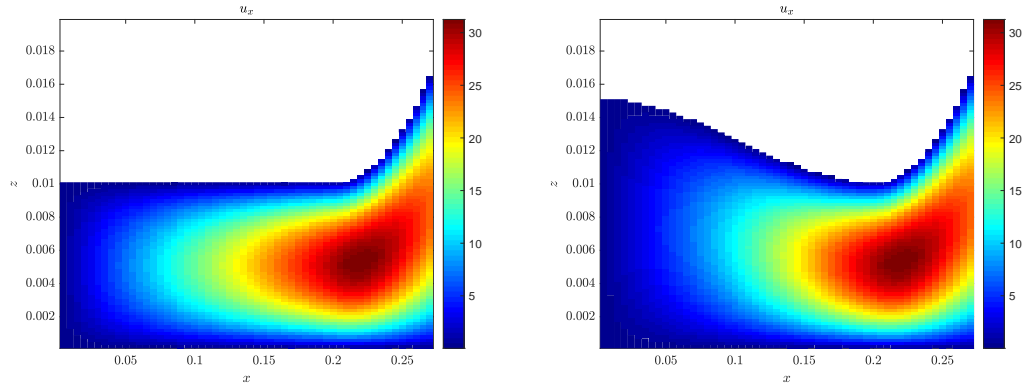


Figure 35: Velocity in  $x$ -direction for the straight interface shape.

Figure 36: Velocity in  $x$ -direction for the dimpled interface shape.

Comparing the wall-normal velocity in figures 37 and 38 shows no significant difference. Fluid moves towards the wall for  $x \leq x_s$  and away from the wall for  $x > x_s$ . The difference in magnitude between the flow in  $x$ -direction and the flow in  $z$ -direction is of more interest. These particular test cases exhibit an order of magnitude difference between the flow directions.

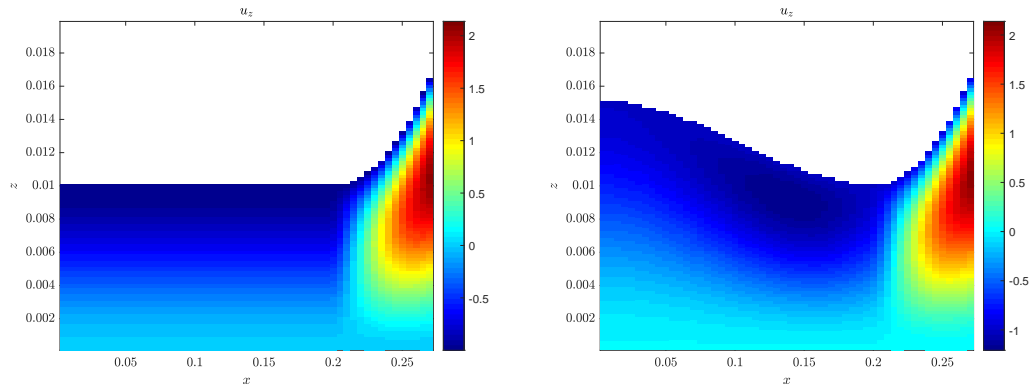


Figure 37: Velocity in  $z$ -direction for the straight interface shape.

Figure 38: Velocity in  $z$ -direction for the dimpled interface shape.

The expression for the wall-normal velocity becomes independent of the distance between the bubble and the wall for negligible curvature (equation (34)), and only depends on the approach speed of the bubble. Meanwhile, the pressure increases as the distance between the bubble and the wall increases, and therefore the derivative of the pressure should increase too, yielding a large value for the wall-tangential velocity. We can therefore expect that the wall-tangential velocity becomes increasingly more dominating compared to the wall-normal velocity as the bubble is nearer to the wall. This holds for areas where curvature is absent or negligible, but might also be true in other areas.

This effect is further demonstrated in figures 39 and 40. These figures show the velocity values for the dimpled shape where  $h_{\min}$  has been decreased by a factor 10 and all other variables

have remained unchanged. It is clear that the difference between the magnitude of the different directions of the flow have increased compared to figures 36 and 38. In addition, the maximum velocity seems more concentrated around the point of minimal distance between the bubble and the wall.

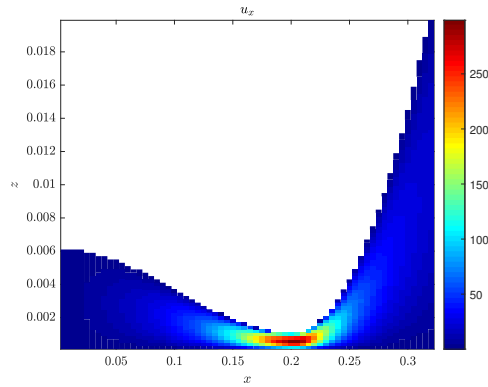


Figure 39: Velocity in  $x$ -direction for a decreased value of  $h_{\min}$ .

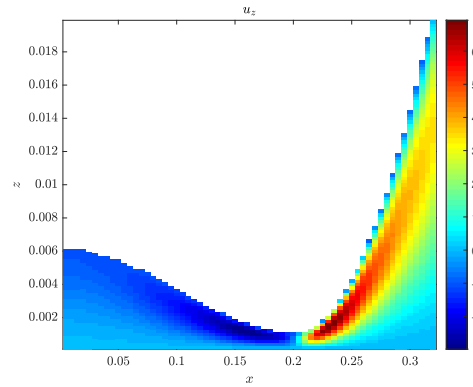


Figure 40: Velocity in  $z$ -direction for a decreased value of  $h_{\min}$ .

To summarize, the results of straight interface shape and the chosen dimpled shape do not show large differences when the dimple height is similar to the distance between the bubble and the wall. The chosen dimple height equals half the minimum distance between the bubble and the wall, whereas physical situations might exhibit relations many times larger. Such a situation shows that the velocity is concentrated around the point of minimal distance and an increase in the difference between the magnitudes of the velocities in the two directions can be observed.

#### 4.6 Application to the case of Heitkam et al.

It is now of interest to apply lubrication theory to the results of section 3. The idea is to take the interface shape and bubble approach speed from the simulation results and subsequently calculate the energy dissipation using lubrication theory. The results can be compared and additionally the quality of the simulation results can be estimated using lubrication theory.

For this purpose the interface shapes at different times have been taken from the simulation data of the case described in section 3.5, as listed below.

- $t = 3.5$ , the bubble is approaching the wall and the flow between the bubble and the wall is assumed to be fully resolved by the solver;
- $t = 3.6$ , there are approximately two grid cells between the bubble and the wall, so the flow is not fully resolved but some properties of the flow should be recognizable;
- $t = 3.7$ , the bubble is within one grid cell of the wall and is approaching it;
- $t = 3.8$ , the bubble is within one grid cell of the wall and is moving away from it.

The shapes at these times are shown in figure 41. The bubble interfaces at these times have been scaled onto the domain  $[0, 1]$  to be applicable to the numerical scheme for the axisymmetrical situation and are displayed such that the plots are consistent with the previous section. The approximated interface shapes are tenth order polynomials obtained using the function *polyfit* in Matlab. A polynomial fit was chosen so that the first and second spatial derivatives are continuous. The deviations of the shape approximations near the right boundary should not pose any problems, since the lubrication pressure at these distances between the bubble and the wall is negligibly small. The wall-normal velocity of the bubble has been chosen as  $w_g$ .

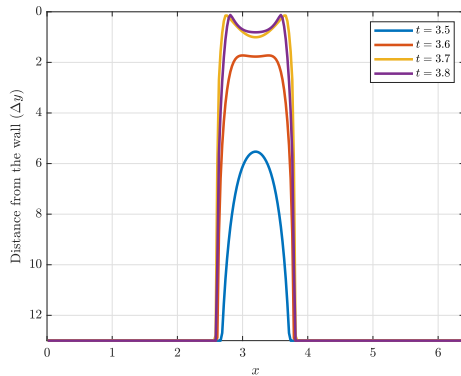


Figure 41: Lamella shapes at different times for the case of Heitkam et al.

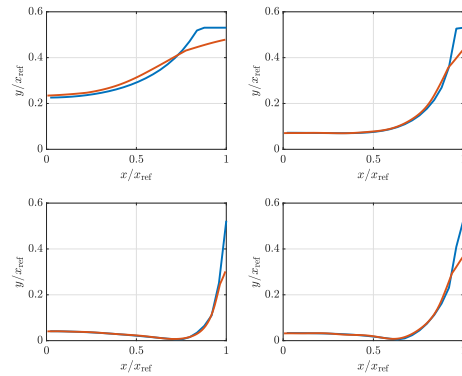


Figure 42: Lamella shapes scaled onto the domain  $[0, 1]$ , given by the blue lines. The red lines are the shapes approximated by tenth order polynomials.

The results for the approximated interfaces shapes are plotted alongside the results from the TBFsolver, as shown in figures 43 to 50. Note that figures containing the results from the TBFsolver are zoomed in on the area between the bubble and the wall, and hence the resolution is low.

These figures reveal that the distribution of dissipation at the wall exhibits similar behaviour for both methods, whereas the distribution of dissipation at the bubble interface shows strong qualitative differences. A possible cause for this is the difference in the boundary conditions for the considered methods. Lubrication theory employs a no-slip condition at the wall and the bubble interface, which results in sharp gradients near the boundaries and hence a large value of the dissipation. The TBFsolver only uses this boundary condition at the wall, which explains the dissipation at the wall. The absence of dissipation at the bubble interface can be explained by the smoothing of the material properties near the interface [6] which yields smoother gradients.

The differences in the magnitude of the dissipation for the considered methods clearly stand out from the presented results. This discrepancy becomes more pronounced as the bubble interface gets closer to the wall.

The large dissipation values in the case of lubrication theory are explained by the distance between the interface and the wall. Equation (49) states that the pressure is proportional to  $h^{-3}$ , indicating large pressures and pressure gradients when  $h$  becomes small. The large pressure gradient induces a large velocity in  $x$ -direction, which yields large velocity gradients due to the

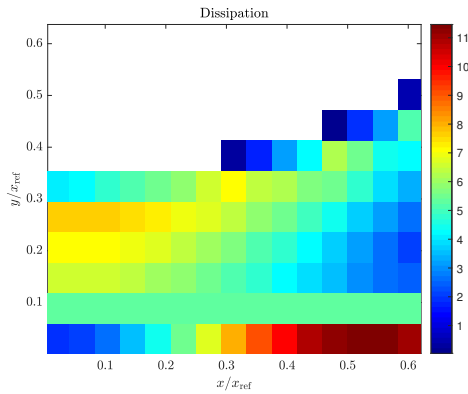


Figure 43: Dissipation obtained from the TBF-solver at  $t = 3.5$ .

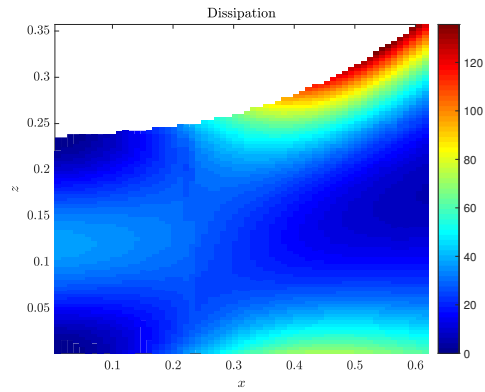


Figure 44: Dissipation obtained from lubrication theory.

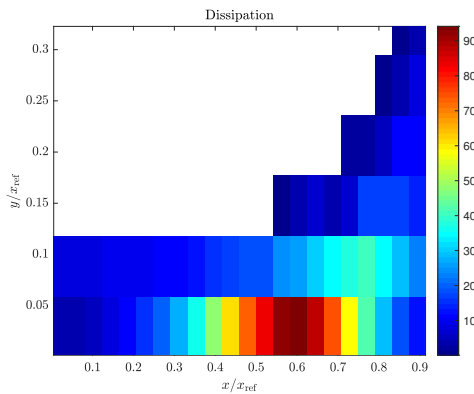


Figure 45: Dissipation obtained from the TBF-solver at  $t = 3.6$ .

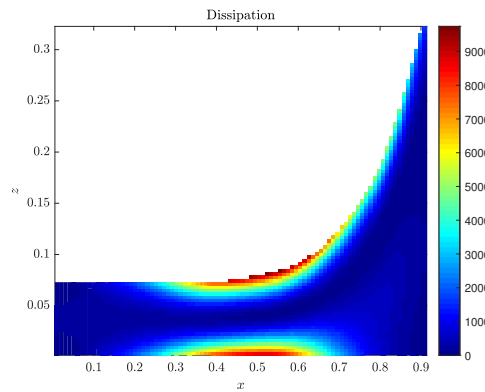


Figure 46: Dissipation obtained from lubrication theory.

boundary conditions at the wall and the bubble interface. These large velocity gradients result in a large value of the dissipation.

It can be argued that the dissipation inside the lamella cannot be extracted properly from the TBFsolver when the bubble is within one grid cell of the wall. Cells at the wall then consist of both the continuous phase and the dispersed phase, and the velocities in these cells are the average of both phases. Hence it is not possible to extract the fluid flow inside the lamella exactly and the calculated dissipation values are inaccurate. The lubrication approximation is based on negligible values of  $H_0$  and  $H_0/R$  and can be considered valid in this situation since  $H_0$  takes on very small values. This would suggest that the results obtained from lubrication theory are more reliable than the results from the TBFsolver when the bubble is within one grid cell of the wall.

A disparity between the two methods is expected when the bubble is further away from the wall, as in figures 43 and 44. For this situation it can be assumed that the results from the TBFsolver are reliable since the flow between the bubble and the wall can be fully resolved. However,  $H_0/R$  takes on a value of approximately 0.23 in figure 43 and can therefore not be

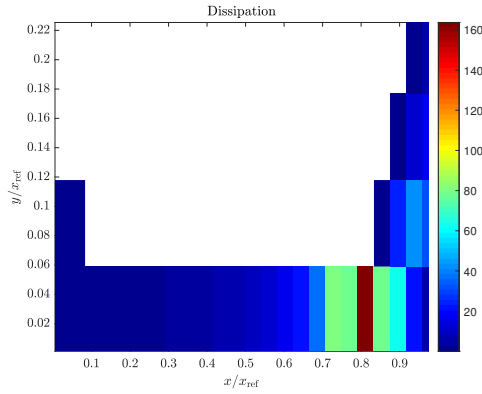


Figure 47: Dissipation obtained from the TBF-solver at  $t = 3.7$ .

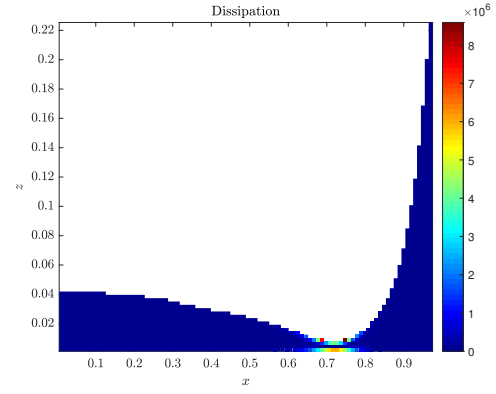


Figure 48: Dissipation obtained from lubrication theory.

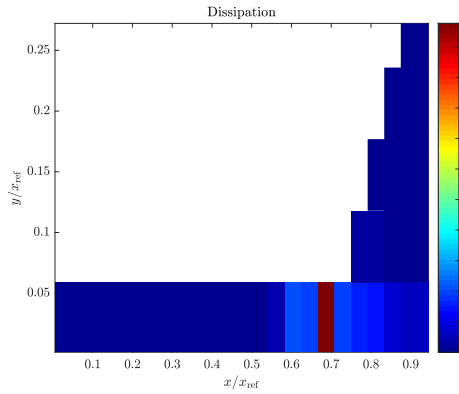


Figure 49: Dissipation obtained from the TBF-solver at  $t = 3.8$ .

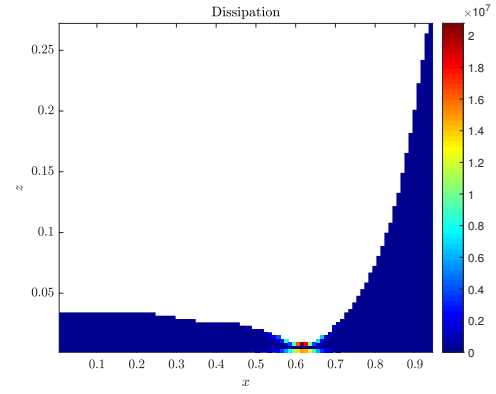


Figure 50: Dissipation obtained from lubrication theory.

considered negligible. This implies that the lubrication approximation is not accurate for this particular situation.

Lubrication theory has been used to estimate the quality of the simulations performed by the TBFsolver. This is done by taking the approximated interface shapes at  $t = 3.7$  and  $t = 3.8$ , when the bubble is within one grid cell of the wall, and subsequently studying the effect of grid refinement in the wall-normal direction on the dissipation distribution. The results of the TBFsolver and lubrication theory seem to show qualitative agreement at these times, and therefore the result of grid refinement for lubrication theory can indicate how much the solution of the TBFsolver can be improved during grid refinement.

The results are shown in figures 51 and 52. The cell sizes are chosen such that they are equal to those used in the TBFsolver. These values correspond to a  $128^3$  grid, a  $256^3$  grid, and a  $512^3$  grid. A reference value of  $R/h = 1000$  is chosen, which equals the cell size corresponding to a  $1280^3$  grid.

The average dissipation for the largest cell size is partially undefined due to the distance be-

tween the bubble and the wall being smaller than the cell size at these points. It is clear that the difference between the results of the coarsest grid and the reference grid are significant. Refining in the wall-normal direction considerably improves the average dissipation. The improvement is most notable at the point of minimal distance. It is unclear what causes the difference at the peak of the the average dissipation for  $R/h = 20$  and  $R/h = 40$ , since the latter generally shows a better approximation to the reference value except at the peak.

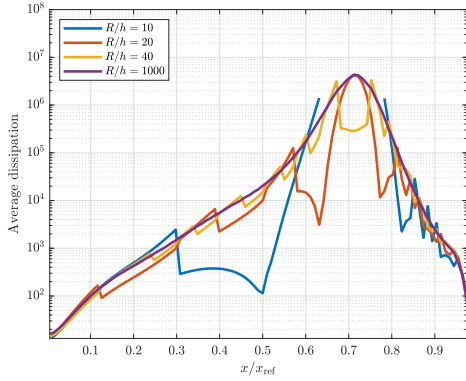


Figure 51: Average dissipation for different cell heights at  $t = 3.7$ .

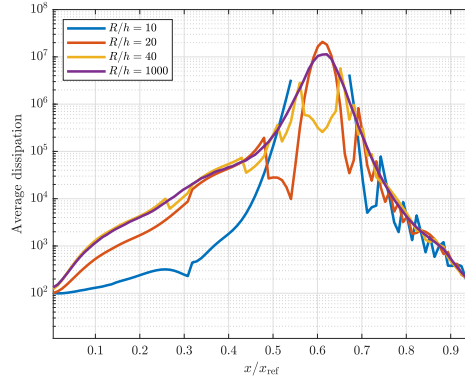


Figure 52: Average dissipation for different cell heights at  $t = 3.8$ .

#### 4.7 Application of lubrication theory to the TBFsolver

DNS becomes computationally expensive when the scales at which lubrication theory is valid have to be fully resolved. The advantage of lubrication theory is that a two-dimensional problem has to be solved to obtain a solution in a three-dimensional situation, allowing the smallest scales to be approximated in a computationally cheap way. This makes implementing lubrication theory into DNS codes an interesting option.

Finding the lubrication pressure forms the basis for the application of lubrication theory to the TBFsolver. It should be noted that the pressure in the gap should by no means replace the pressure which follows from the Poisson equation in the solver, but rather it should influence the provisional velocity per time stage. This would keep the velocity field at the end of each time stage divergence free. Incorporating the lubrication pressure into the provisional velocity can intuitively be done in two ways.

- Imposing the movement of the bubble interface using equation (43).
- Inserting a local lubrication force into the Navier-Stokes equations.

##### Imposing the interface movement

Imposing the interface movement affects the advection of the marker function. This means that the Navier-Stokes equations remain unchanged and a divergence-free velocity field is obtained at the end of each time stage. However, altering the advection of the marker function (equation 1) does not guarantee mass conservation. This poses a major problem and hence this approach is not recommended unless a clever way to correct for the change of mass is found.

### Inserting a local lubrication force

Defining a lubrication force on the bubble interface can be done similar to the method of Zhang and Law [23]. An axisymmetrical situation is assumed in their case which allows for calculating a lubrication force on the entire bubble. The lubrication force is calculated as the lubrication pressure integrated over the area:

$$F_{\text{lub}} = \int_A p_{\text{lub}} \, dA. \quad (60)$$

Due to the numerical methods used in the TBFsolver and the solution of the Reynolds equation, the logical choice of  $A$  would be a single computational cell. The lubrication force would then be defined per cell and added as a term to the nondimensional Navier-Stokes equations used by the TBFsolver.

The main advantage of this method is that crucial parts of the numerical algorithm of the TBFsolver remain untouched, these parts being the marker advection function and the fractional step time integration. Adding an additional term to the Navier-Stokes equations does influence the provisional velocity and eventually the pressure distribution, but the velocity field at the end of each time stage remains divergence-free.

Care should be taken when applying  $F_{\text{lub}}$ . We should ideally have that the total pressure equals the sum of the ambient pressure and the lubrication pressure in cells between the bubble and the wall where only liquid is present. When a cell contains the bubble interface, the provisional velocity, hence the pressure as well, depends on the averaged material properties in the cell. Therefore the space between the bubble and the wall is already accounted for in these cells and applying an additional force would then not be physically correct.

## 4.8 Concluding remarks

In this section we approached bubble-wall interactions from a theoretical point of view. The asymptotic aspect ratio that naturally occurs during these interactions allows for the simplification of the Navier-Stokes equations into the Reynolds equation, which forms the basis for lubrication theory. This equation reduces a three-dimensional problem into an computationally cheaper two-dimensional problem and takes the smallest scales of the flow into account.

Applying lubrication theory to a straight and dimpled interface shape showed no significant differences as long as the dimple height is of the same order as the minimal distance between the wall and the bubble interface.

Comparison between the result of lubrication theory and the TBFsolver resulted qualitative agreement, but large quantitative differences. The qualitative agreement is best visible at the wall, where the boundary conditions of both methods are the same. The lack of qualitative agreement at the bubble interface is likely caused by smoothing of material properties at these points. A possible explanation for the quantitative differences is the inaccurate extraction of sub-grid processes from the TBFsolver.

Lubrication theory has also been used to estimate the quality of the solution of the TBFsolver. The method implies that a substantial improvement occurs when refining from a  $128^3$  grid to a  $256^3$  grid for the considered case. These improvements are most notable near the point of minimal distance.

---

## 5 Conclusions

The goal of this thesis was to investigate bubble-wall interactions using direct numerical simulation. These interactions occur frequently in applications where bubbly flows are present, making it important to understand the behaviour of bubbles when they collide with a wall.

The numerical program TBFsolver has been used to perform the simulations. Accurately simulating these interactions is not trivial due to the small-scale processes taking place. For this reason a grid refinement study and a comparison to experimental results of a bubble-wall interaction and an existing bubble collision model have been performed in section 3. The physical experiment could be recreated well and grid refinement indicated that the results of the TBFsolver were reliable.

Assumptions in the bubble collision model of Heitkam et al. regarding the bubble deformation during contact with the wall and the distribution of energy dissipation have been compared to the results of the TBFsolver. The proposed relation between the contact area and the distance to the wall exhibited a significant difference compared to the simulation results. The majority of the energy dissipation was found to take place near the rim of the contact area between the bubble and the wall, as proposed by the collision model. Results suggested that a significant amount of energy dissipation also takes place in the fluid lamella between the bubble and the wall.

Lubrication theory was used in section 4 to approach bubble-wall interactions from a theoretical perspective. This approach makes use of the asymptotic aspect ratio of the length scales present when the bubble is close to the wall in order to simplify the Navier-Stokes equations. Expressions for the flow inside the fluid lamella were found and have been used to reconstruct the flow based on the simulation data of the TBFsolver. Lubrication theory predicts a strong peak in the energy dissipation concentrated around the point of minimal distance between the bubble and the wall. Comparing the simulation results to the results of lubrication theory showed qualitative agreement, but large quantitative differences. These differences are assumed to be partially caused by inaccuracies in the extraction of data from the TBFsolver in the fluid lamella. The results from this section are inconclusive due to the uncertainties in processing the simulation data.

The section on lubrication theory concludes with a brief discussion on a possible implementation of the theory into the TBFsolver. The most viable option is to include a local lubrication force based on the lubrication pressure, as this method leaves the framework of the TBFsolver mostly unchanged.



---

## 6 Discussion and recommendations

A list of choices made throughout the report and related recommendations is given below.

### **The choice of the numerical code**

It had already been determined at the start of the project that the TBFsolver would be used to perform numerical simulations of multiphase flows. The code was readily available and contact with the developer was possible. Moreover, the code had already been tested for situations involving both single bubbles and multiple bubbles and therefore seemed a good choice for solving multiphase flows. There are undoubtedly many other numerical codes for solving multiphase flows which can also simulate bubble-wall or bubble-bubble interactions. It would be interesting if a certain benchmark test for these interactions could be designed in order to compare the various numerical programs, similar to benchmark tests for rising bubbles in two-dimensional solvers [13] and three-dimensional solvers [1].

### **The choice of the bubble collision model**

Using the results of Heitkam et al. for comparison with the TBFsolver was a logical choice given the contact with the group of Fluid Mechanics at the TU Dresden at the time the project started. The availability of experimental data made it easier to verify the choice of input parameters for the code. In addition, there were several assumptions made for the proposed model that allowed for good comparison with results of the TBFsolver.

### **Grid refinement and computational costs for comparing to lubrication theory**

Two distinct cases for the same set of variables were considered in section 3, for which two grids were employed. An additional grid refinement is necessary to substantiate or invalidate the results obtained in the mentioned section. This refinement was planned but could unfortunately not be completed due to time limitations. Instead, this task will be performed in the months after this final project has been completed.

It must be noted that a  $512^3$  grid for the considered case is the finest grid which is practically feasible for numerical simulation. It is therefore recommended to use a numerical program which either solves a two-dimensional flow or an axisymmetrical flow. This significantly reduces computational costs whilst allowing for the same comparison between numerical simulation data and predictions from lubrication theory. In addition, using a finer grid would reduce the uncertainty in extracting the data from the numerical solver when comparing to lubrication theory.

### **Energy dissipation inside the bubble**

Throughout this report we have only investigated the energy dissipation inside the fluid. The main motivation for this was for comparison with the model proposed by Heitkam et al. Flow and energy dissipation inside the bubble can also be investigated in addition to the energy dissipation inside the fluid, in order to obtain a more complete understanding of the processes that take place during bubble-wall interactions. The energy dissipation inside the bubble during

periods of strong deformation are then of special interest. Subsequent comparisons between existing models be made, for instance with the bubble energy dissipation model of Zhang and Law [23].

### **The uncertainty in defining the fluid lamella**

It is unclear how the fluid lamella should be defined exactly, as stated in section 3. A threshold value  $c_{th}$  for the volume fraction field was introduced to make it possible to properly compare the results on different grids. It is likely that the desired value of  $c_{th}$  depends on the considered situation, just as the lamella thickness is expected to depend on the material properties of the both phases. Ideally, the lamella thickness should be investigated by performing physical experiments. The same experiments can be performed numerically in order to verify how well the numerical program deals with the small scales that occur during bubble-wall interactions. These tests can substantiate the numerical results of cases which have not been tested experimentally.

## Bibliography

- [1] J. Adelsberger, P. Esser, M. Griebel, S. Gross, M. Klitz, and A. Ruttgers. 3D Incompressible Two-Phase Flow Benchmark Computations for Rising Droplets. *World Congress on Computational Mechanics*, l(1401):14, 2014.
- [2] S. Afkhami and M. Bussmann. Height functions for applying contact angles to 3D VOF simulations. *International Journal for Numerical Methods in Fluids*, 61(8):827–847, 2009. doi: 10.1002/fld.1974. URL <https://onlinelibrary.wiley.com/doi/abs/10.1002/fld.1974>.
- [3] D Berthe and M Godet. A more general form of reynolds equation–application to rough surfaces. *Wear*, 27(3):345–357, 1974.
- [4] J.U Brackbill, D.B Kothe, and C Zemach. A continuum method for modeling surface tension. *Journal of Computational Physics*, 100(2):335 – 354, 1992. ISSN 0021-9991. doi: [https://doi.org/10.1016/0021-9991\(92\)90240-Y](https://doi.org/10.1016/0021-9991(92)90240-Y). URL <http://www.sciencedirect.com/science/article/pii/002199919290240Y>.
- [5] P. Cifani, J.G.M. Kuerten, and B.J. Geurts. Highly scalable DNS solver for turbulent bubble-laden channel flow. *Computers and Fluids*, 172:67 – 83, 2018. ISSN 0045-7930. doi: <https://doi.org/10.1016/j.compfluid.2018.06.008>. URL <http://www.sciencedirect.com/science/article/pii/S0045793018303311>.
- [6] Paolo Cifani. *DNS of turbulent bubble-laden channel flows*. PhD thesis, University of Twente, 2017.
- [7] Sharen J. Cummins, Marianne M. Francois, and Douglas B. Kothe. Estimating curvature from volume fractions. *Computers and Structures*, 83(6):425 – 434, 2005. ISSN 0045-7949. doi: <https://doi.org/10.1016/j.compstruc.2004.08.017>. URL <http://www.sciencedirect.com/science/article/pii/S0045794904004110>. Frontier of Multi-Phase Flow Analysis and Fluid-Structure.
- [8] Robert H Davis, Jeffrey A Schonberg, and John M Rallison. The lubrication force between two viscous drops. *Physics of Fluids A: Fluid Dynamics*, 1(1):77–81, 1989.
- [9] Marianne M. Francois, Sharen J. Cummins, Edward D. Dendy, Douglas B. Kothe, James M. Sicilian, and Matthew W. Williams. A balanced-force algorithm for continuous and sharp interfacial surface tension models within a volume tracking framework. *Journal of Computational Physics*, 213(1):141 – 173, 2006. ISSN 0021-9991. doi: <https://doi.org/10.1016/j.jcp.2005.08.004>. URL <http://www.sciencedirect.com/science/article/pii/S0021999105003748>.
- [10] BD Goddard, RD Mills-Williams, and J Sun. Exact solutions and asymptotics for the hydrodynamic interaction between two unequal collinear spheres in viscous fluid. *arXiv preprint arXiv:1809.05459*, 2018.
- [11] Jingchen Gu, Motoki Sakaue, Shintaro Takeuchi, and Takeo Kajishima. An immersed lubrication model for the fluid flow in a narrow gap region. *Powder Technology*, 329:445–454, 2018.
- [12] Sascha Heitkam, Anna Elisabeth Sommer, Wiebke Drenckhan, and Jochen Fröhlich. A simple collision model for small bubbles. *Journal of Physics Condensed Matter*, 29(12), 2017. ISSN 1361648X. doi: 10.1088/1361-648X/aa56fc.

- [13] S. Hysing, S. Turek, D. Kuzmin, N. Parolini, E. Burman, S. Ganesan, and L. Tobiska. Quantitative benchmark computations of two-dimensional bubble dynamics. *International Journal for Numerical Methods in Fluids*, 60(11):1259–1288, 2018.
- [14] Pijush K Kundu, Ira M Cohen, and DW Dowling. *Fluid mechanics 4th*, 2008.
- [15] B.P. Leonard. A stable and accurate convective modelling procedure based on quadratic upstream interpolation. *Computer Methods in Applied Mechanics and Engineering*, 19(1):59 – 98, 1979. ISSN 0045-7825. doi: [https://doi.org/10.1016/0045-7825\(79\)90034-3](https://doi.org/10.1016/0045-7825(79)90034-3). URL <http://www.sciencedirect.com/science/article/pii/0045782579900343>.
- [16] Jiakai Lu and Gretar Tryggvason. Numerical study of turbulent bubbly downflows in a vertical channel. *Physics of Fluids*, 18(10):103302, 2006. doi: 10.1063/1.2353399. URL <https://doi.org/10.1063/1.2353399>.
- [17] G. D. M. Mackay and S. G. Mason. The gravity approach and coalescence of fluid drops at liquid interfaces. *The Canadian Journal of Chemical Engineering*, 41(5):203–212, 1963. doi: 10.1002/cjce.5450410504. URL <https://onlinelibrary.wiley.com/doi/abs/10.1002/cjce.5450410504>.
- [18] Rogerio Manica, Maurice H.W. Hendrix, Raghvendra Gupta, Evert Klaseboer, Claus-Dieter Ohl, and Derek Y.C. Chan. Modelling bubble rise and interaction with a glass surface. *Applied Mathematical Modelling*, 38(17):4249 – 4261, 2014. ISSN 0307-904X. doi: <https://doi.org/10.1016/j.apm.2014.03.039>. URL <http://www.sciencedirect.com/science/article/pii/S0307904X14001425>.
- [19] Gosse Oldenziel. *Droplet collisions in turbulence*. PhD thesis, TU Delft, 2014.
- [20] J. Qian and C. K. Law. Regimes of coalescence and separation in droplet collision. *Journal of Fluid Mechanics*, 331, 1997. doi: 10.1017/S0022112096003722.
- [21] Alessandro Ruggiero, Emilio Gomez, and Roberto DAmato. Approximate analytical model for the squeeze-film lubrication of the human ankle joint with synovial fluid filtrated by articular cartilage. *Tribology letters*, 41(2):337–343, 2011.
- [22] JM Skotheim and Laksminarayanan Mahadevan. Soft lubrication. *Physical review letters*, 92(24):245509, 2004.
- [23] Peng Zhang and Chung K Law. An analysis of head-on droplet collision with large deformation in gaseous medium. *Physics of Fluids*, 23(4):042102, 2011.

## A Nomenclature

### A.1 Variables and vectors

A list of used variables with their definition and dimension is given below. Here  $L$  denotes length,  $M$  denotes mass, and  $T$  denotes time.

$\alpha$	angle of gravity	
$\varepsilon$	energy dissipation	$L^2T^{-3}$
$\mu$	viscosity	$ML^{-1}T^{-1}$
$\rho$	density	$ML^{-3}$
$\sigma$	surface tension	$MT^{-2}$
$\Delta\rho$	density difference	$ML^{-3}$
$\Delta x$	grid size	$L$
$c$	volume fraction field	
$c_{\text{th}}$	volume fraction threshold value	
$h$	grid size (section 3)	$L$
$h$	interface-wall distance (section 4)	$L$
$h_{\text{min}}$	minimum interface-wall distance	$L$
$p$	pressure	$ML^{-1}T^{-2}$
$g$	gravitational acceleration	$LT^{-2}$
$R$	bubble radius	$L$
$R_a$	equivalent radius of contact area	$L$
$t$	time	$T$
$\mathbf{u}$	velocity vector ( $u, v, w$ )	
$u$	velocity in $x$ -direction	$LT^{-1}$
$v$	velocity in $y$ -direction	$LT^{-1}$
$w$	velocity in $z$ -direction	$LT^{-1}$
$\mathbf{x}$	position vector ( $x, y, z$ )	
$\mathbf{x}_c$	bubble center of mass vector ( $x_c, y_c, z_c$ )	
$x, y, z$	coordinates	$L$
$x_c, y_c, z_c$	bubble center of mass coordinates	$L$

### A.2 Dimensionless numbers

The table below gives an overview of the dimensionless numbers used throughout this thesis, along with the definition and interpretation of each number. Here  $U$  denotes a characteristic velocity and  $L$  denotes a characteristic length.

Eo	Eötvös number	$\Delta\rho g L^2 / \sigma$	ratio of gravitational forces to surface tension forces
Fr	Froude number	$U / \sqrt{gL}$	ratio of inertial forces to gravitational forces
Ga	Galilei number	$\rho_1 \sqrt{ \rho_2 / \rho_1 - 1  g L^3} / \mu_1$	ratio of gravitational forces to viscous forces
Re	Reynolds number	$UL\rho / \mu$	ratio of inertial forces to viscous forces
We	Weber number	$LU^2\rho / \sigma$	ratio of inertial forces to surface tension forces